NTNU

Norwegian University of
Science and Technology

Engineering Quantum States in δ-doped Semiconductors

Ann Julie Utne Holt

Master of Science
Submission date: July 2017
Supervisor: Justin Wells, IFY

Norwegian University of Science and Technology
Department of Physics

Abstract

By creating phosphorus δ-layers in silicon, varying in thickness from an atomically sharp doping profile to a 4.0 nm layer, the effect of quantum confinement on the electronic structure of a 2DEG was studied using ARPES. The location of theoretically predicted, but experimentally undiscovered, quantum well states known as 1Δ was revealed, validating density functional theory calculations developed for describing Si:P δ-layer systems. Verification of these states contributes to the development of accurate models describing the behaviour of δ-layer derived devices. Further, the electronic band structure of boron-doped thin film (1.8 nm) diamond was uncovered and compared to that of thick film (> 3 μm). Although diamond and silicon share several crystallographic properties, it was found that confinement induced different effects in these materials. Two-dimensional electron states were induced in silicon already for dopant layers of 4.0 nm, and a valley splitting of 120 meV was created between the two most occupied bands upon reaching a 2.0 nm doping profile. A confinement of 1.8 nm was shown to have little effect on the diamond band structure, however. The surface δ-doped thin film displayed negligible differences from its bulk counterpart, supporting the notion of utilising thin film diamond in miniaturised systems.

Sammendrag

Den kvantemekaniske effekten av δ-doping i silisium har blitt studert ved bruk av "angle-resolved photoemission spectroscopy", ARPES. Dette ble gjort ved å danne fosfor δ-lag med dopingsprofiler varierende i tykkelse fra ett atomlag til 4.0 nm. Målingene førte til bekreftelse av teoretisk forventede, men hittil ikke påviste elektrontilstander, kjent som 1Δ. Den eksperimentelle verifikasjonen av disse tilstandene styrker teoretisk utviklede modeller, og kan dermed medvirke til en mer presis modellering av komponenter basert på Si:P δ-doping. Båndstrukturene til tynnfilm (1.8 nm) og tykkfilm (>3 μm) p-dopet diamant har også blitt direkte målt ved bruk av ARPES. Til tross for at diamant og silisium deler flere krystallografiske egenskaper, har det blitt vist at disse materialene ble svært forskjellig påvirket av en tynn dopingsprofil. Todimensjonale elektrontilstander ble påvist i silisium ved profiler på 4.0 nm, og en 120 meV energisplitting oppstod mellom de to mest okkuperte tilstandene ved en profil på 2.0 nm. Diamant derimot, viste en overraskende liten effekt av begrensningene indusert av δ-doping, da båndstrukturen innhentet fra tynnfilm diamant fremstod som ubetydelig endret sammenlignet med tykkfilm diamant. Dette resultatet tyder på at egenskapene til diamant vil være bevart i miniatyriserte systemer.

Preface

This thesis concludes my studies at the Norwegian University of Science and Technology (NTNU) within the physics teacher education program. The work presented here is the result from beamtimes at three different synchrotrons; a two-week experiment at the Aarhus storage ring in Denmark (ASTRID), one week at Elettra Synchrotron in Trieste, Italy, and lastly a trip to the Swiss Light Source (SLS) in Switzerland. The work with this thesis have consisted of interpreting and analysing the ARPES measurements, understanding the techniques used, and learning how to run a synchrotron beamline.

I would like to thank my supervisor Justin Wells for his endless support and encouragement. His interest in others learning and his thorough explanations has been motivating and invaluable. By creating an including atmosphere, where a whole research group may work as a unit, he truly makes a great environment for a master student to work and learn exciting new physics. I am also very grateful to postdoc Simon Cooil who has taught me to value the practical aspects of an experiment, as well as the theory. Not only is he skilled at running the lab, but he also fixes and builds new instrument parts, encouraging people around him. Lastly, I would like to thank postdoc Alex Schenk who have aided me in everything from writing code to staying awake during beamtimes. His willingness to help and give explanations (at any hour of the day) has been of great importance. Thank you.

Trondheim, 2017

Ann Julie Utne Holt

Contents

List of Figures

Abbreviations

2DEG two-dimensional electron gas

ARPES Angle-Resolved Photoemission Spectroscopy

ASTRID Aarhus storage ring in Denmark

BZ Brillouin zone

CBM conduction band minimum

DFT density functional theory

EDC energy distribution curve

ML monolayer

NTNU Norwegian University of Science and Technology

PES Photoemission Spectroscopy

PP pseudopotential method

SLS Swiss Light Source

TB tight-binding

UHV ultra high vacuum

VBM valence band maximum

Chapter 1

Introduction

The manufacturing of small device structures requires that the spatial distribution of material dopants are well controlled, and the mechanisms involved in this concept must be understood on a near atomic-length scale. The first clear evidence for a narrow doping profile, known as δ-doping, was presented in 1984 by Schubert *et al* [45], showing a full doping profile width of 4.0 nm epitaxially grown Si on GaAs. The theoretical limit of confining dopants to a single atomic plane in the host material has now been reached, and δ-doping has proven to be a successful approach for creating a new class of electronic devices [6]. Today, δ-doping has greatly contributed to the insight in reduced dimension electronics [16], it has been used to realise the making of the worlds smallest transistor [18], and is now considered a promising platform for quantum computing components [55]. The possibility of doping with atomic level precision introduces a new era in device manufacturing. Following this, new understanding needs to be developed, as quantum confinement effects begin to show their influence. In this thesis, δ-doping has been investigated in two materials; silicon and diamond.

Being both a semiconductor and an abundant element on Earth, silicon has become one of the most widely used materials for device manufacturing. When the recent achievement of δ-doping is realised in silicon, creating a hybrid material with metallic properties, silicon becomes a natural candidate for future quantum computer devices. This requires the engineering of suitable quantum states in a host material, which must be controlled, manipulated and read with atomic-scale precision. The presented experiment investigate the quantum confinement effects induced in silicon when a dopant layer of phosphorus is reduced from a 4.0 nm profile down to a single atom layer. This is conducted with the specific goal of

verifying the formation of theoretically calculated quantum well states, known as 1Δ, a prediction not yet experimentally confirmed. Precise knowledge of these states may show crucial for an accurate model of the behaviour of δ-layer derived devices, making an experimental verification of these states desirable.

Diamond has gained industrial attention in its own right. It is one of the hardest materials existing in nature, holds the highest recorded value for thermal conductivity [41], it displays high breakdown field strength, and high carrier mobility. Diamond is an electrical insulator, but shown to obtain superconductive behaviour upon doping boron in concentrations exceeding $5 \cdot 10^{20}$ cm^{-3} [6]. These superior properties are desirable to maintain for nanoscale systems. Little is known about the electronic band structure of thin film diamond, largely due to the difficulties of creating sufficiently high quality samples [17]. The experiment presented aims to contribute to this missing information, as significant progress in the fabrication of δ-doped diamond is recently shown [6]. Using angle-resolved photoemission spectroscopy, the electronic band structure of metallic diamond at the nanometer scale is uncovered, investigating the effect of confinement and the usage of diamond in miniaturised systems.

The process of δ-doping, together with a theoretical basis regarding the electronic behaviour of crystals, is presented in Chapter 2. The effect of δ-doping confinement is studied using the technique of angle-resolved photoemission spectroscopy. Chapter 3 is therefore dedicated to the theoretical concepts surrounding this experimental technique, and Chapter 4 describes the associated experimental requirements and methods. The results obtained will be presented in two parts; the investigation of silicon δ-layers will be presented in Chapter 5, while Chapter 6 is dedicated to diamond thin- and thick- film. Narrow doping profiles in silicon have already been intensely studied, and this thesis aims to address some unanswered questions within this field. Before the results are presented, the specifics of these questions are elaborated on in Chapter 5, together with a description of the adapted experimental approach. Little is known about the electronic structure of δ-doped diamond, but an introduction of earlier works is provided prior to the results in Chapter 6. The results are discussed as they are presented, together with suggestions for further work. Some speculations regarding the different observed effect of δ-doping in the two materials are offered last in Chapter 6 and the conclusions are summarised in Chapter 7.

Chapter 2

Theory

This chapter provides a basis for some of the theoretical aspects of the work presented in this thesis. The ideas described here concern the electrical properties of materials, while the next chapter addresses methods used to measure such properties. A description of the electronic band structure is presented, developed from the nearly free electron model. Different electronic states are discussed within this framework, and it will be shown that the concept of δ-doping may give rise to new exciting electronic states in a material.

2.1 Electrons in a crystal

In order to exploit the electronic properties of a material, it is necessary to have some understanding of the electrons residing there. The better our understanding, the greater are the possibilities for creative developments. The most accurate description of particles available today is provided by the famous Schrödinger equation, named so after its developer Erwin Schrödinger. In its time-independent form, this equation reads

$$\left[\frac{-\hbar^2}{2m}\nabla^2 + U(\boldsymbol{r})\right]\psi(\mathbf{r}) = E\psi(\boldsymbol{r}), \tag{2.1}$$

where $\psi(\boldsymbol{r})$ is the *wavefunction* describing the particle, E is the particle energy, and $U(\boldsymbol{r})$ is the surrounding potential. The constants m and $\hbar$ are the particle

mass and the reduced Planck constant respectively, while $\boldsymbol{r}$ is the spatial coordinate. To describe the behaviour of electrons, we thereby need to know what potential, $U(\boldsymbol{r})$, surrounds them. The precise form of $U(\boldsymbol{r})$ is usually unknown, but in a crystal we can take advantage of the fact that the potential must have the *same periodicity* as the crystal lattice [24]. When imposing this condition, $U(\boldsymbol{r}) = U(\boldsymbol{r} + \boldsymbol{R})$, where $\boldsymbol{R}$ is a crystal lattice vector, the general solution to 2.1 becomes the familiar *Bloch waves* [1],

$$\psi_{\boldsymbol{k}}(\boldsymbol{r}) = u_{\boldsymbol{k}}(\boldsymbol{r})e^{-i\boldsymbol{k}\cdot\boldsymbol{r}}, \tag{2.2}$$

where $u_{\boldsymbol{k}}(\boldsymbol{r})$ is a lattice periodic function. The vector $\boldsymbol{k}$ is a measure of the momentum[2] carried by the electron, and is used to label the different Bloch wave solutions. By analysing the wavefunction, it is evident that this is in fact periodic with the *reciprocal lattice*, so that $\psi_{\boldsymbol{k}}(\boldsymbol{r}) = \psi_{\boldsymbol{k}+\boldsymbol{G}}(\boldsymbol{r})$, where $\boldsymbol{G}$ is a reciprocal lattice vector. Inserting back into the Schrödinger equation, we see that this also must apply for the energy, so

$$E_{\boldsymbol{k}} = E_{\boldsymbol{k}+\boldsymbol{G}}. \tag{2.3}$$

This means that it is not necessary to examine $\psi_{\boldsymbol{k}}(\boldsymbol{r})$ and $E_{\boldsymbol{k}}$ for all values of $\boldsymbol{k}$, but we can restrict ourselves to an analysis of just the first Brillouin zone (BZ)[3]. One might think that inside a material there will for certain exist *some* electrons carrying any given energy. However, it turns out that this is not the case. Inside a crystal, the different energy values follow a specific pattern, and some values of energy are not carried by *any* electrons. This is one of the key properties of a crystal, and is exploited in most everything of modern electronics. It is therefore of great interest to describe and, even better, manipulate the different energy values allowed in a material. By plotting which energies are associated with electrons of a specific momentum, $E(\boldsymbol{k})$, we obtain what is commonly called the *electronic band structure* of the material [29].

[1] *"By straight Fourier analysis I found to my delight that the wave differed from the plane wave of free electrons only by a periodic modulation."* -F. Bloch.

[2] Note that $\boldsymbol{k}$ is just a *measure* of the momentum, $\boldsymbol{p}$, carried by the electron. The actual momentum is given by $\boldsymbol{p} = \hbar\boldsymbol{k}$

[3] A derivation of the Bloch wavefunctions and the Brillouin zone together with a thorough explanation of the concepts surrounding these are provided by Ref. [29].

2.2 Band structure of crystals

How can we find this band structure we are interested in? Firstly, we need a theoretical basis to develop our understanding. There are several ways to obtain an intuitive understanding of the band structure, the approach elaborated here being the *nearly free electron model*. In this model, we first consider the solution of the Schrödinger equation for a truly free electron; that is, an electron moving in the potential $U(\boldsymbol{r}) = 0$. Such an electron may take on any energy value, as shown in Figure 2.1a, where the function of $E(\boldsymbol{k})$ becomes a mere parabola centred at $\boldsymbol{k} = 0$[4]. We can now proceed by assuming the periodic potential is *almost* zero, so that the electrons are nearly free. For the solutions, we obtain the same parabola as for the free electron, but now we also get repeated parabolas, separated by $\boldsymbol{G}$, which meet the requirement of Eqn. 2.3. These solutions are shown in Figure 2.1b. The situation now has dramatically changed. Where before, a given value of $\boldsymbol{k}$ had only one associated value of E corresponding to a solution of the Schrödinger equation, now there are several (in principle infinite for an infinite crystal).

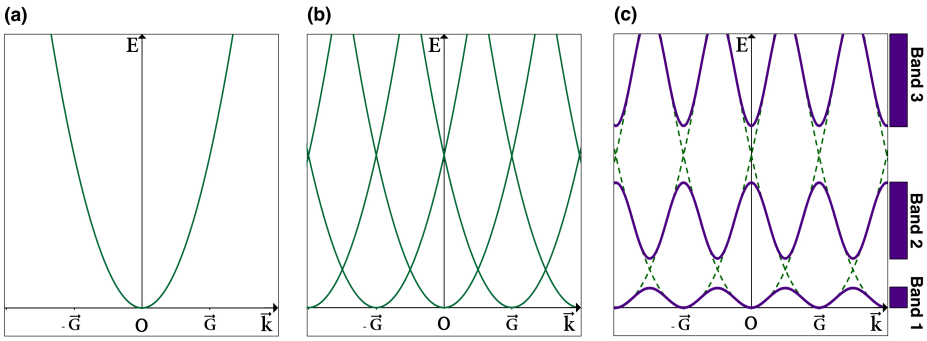

Figure 2.1: *Nearly free electron model.* (a) Situation for a truly free electron. There exists a solution to the Schrödinger equation for all values of energy, E. (b) Electron in an almost vanishing periodic potential. Same solutions as for a free electron, now also repeated with the reciprocal lattice. (c) Effect of increasing the potential strength. Gaps open near the zone boundaries, giving rise to the formation of bands. Figure adapted from Ref. [26].

An interesting effect occurs as we let the potential strength slowly increase. This situation is shown in Figure 2.1c, where the solutions from (b) are represented

[4]The same solutions also hold for non-zero potential, as long as the potential is constant.

by dotted green lines. We find that the solutions start to change in such a way that *gaps* begin to appear in the Figure. That is, some values for E no longer have a corresponding value of $\boldsymbol{k}$ that yield a solution to the Schrödinger equation. These are known as *forbidden* energy values, and no electron in the crystal can have this energy. The range of energy values where solutions do exist, form what is known as the electron *bands* in the crystal. Each band is in reality made up of a discrete set of allowed energy values, where each atom contributes to a singular value. The bands only form a true continuum for an infinite crystal, but in most situations the number of atoms in the system is so large as to make little difference from the idealised situation [49].

The situation in a crystal is now this: the electrons can only possess certain energy values. These values are clustered so close together as to form a continuum of allowed energies, broken apart with periods where no solution to the Schrödinger equation exists. These are known as *bands* and *gaps* respectively. This finding has been of fundamental importance in solid state physics, where it has been successfully used to explain many physical properties, such as electrical conductivity in semiconductors, optical transparency and magnetotransport. It provides a clear distinction between metals, semiconductors and insulators, and forms the understanding of all solid-state devices [29]. As an example of the powerful insight that follows from the band description of materials, consider this somewhat simplified illustration: Imagine a material where all the solutions within the first two bands in Figure 2.1c are filled with an electron. Visible light shines upon the material, that is, the material is hit by photons of a given energy within the range of visible light. An electron may absorb a photon and get lifted to a higher energy state. According to the Pauli exclusion principle, no two electrons may occupy the same quantum state within the system simultaneously. When all the states in band 1 and band 2 are filled, the next available state is in the bottom of band 3. What then happens if the photons hitting this material do not carry enough energy to lift an electron up to band 3? The answer is that no electron will absorb the photons, which in turn will pass unaffected through the material. Thus, this material will appear optically transparent [48]. The band description of materials thus offers an intuitive understanding of why some materials are transparent and others not.

2.3 Bulk- and surface states

We now understand that inside a crystal there are some values of energy in which there exists a solution to the Schrödinger equation, and others where there does not. We can now proceed with investigating what these solutions, $\psi_{\boldsymbol{k}}(\boldsymbol{r})$,

look like. Inside a crystal, the periodic potential demands that these solutions are Bloch waves, as previously described. When investigating the form of these (Eqn. 2.2), we see that they are periodic oscillating waves, stretching out infinitely in all directions. Interpreting $|\psi_{\boldsymbol{k}}(\boldsymbol{r})|^2$ as the *position probability density* we understand that this cannot be the end of the story, as it would imply that the wavefunction does not change as it stretches outside the crystal. The electrons are bound to the solid (or, more precisely, we only consider the bound electrons), so outside the crystal the wavefunction must take on a decaying form. By appropriately matching a Bloch wave inside the solid with an exponentially decay [5] in vacuum, we get the description of a *bulk state*, as shown in Figure 2.2a.

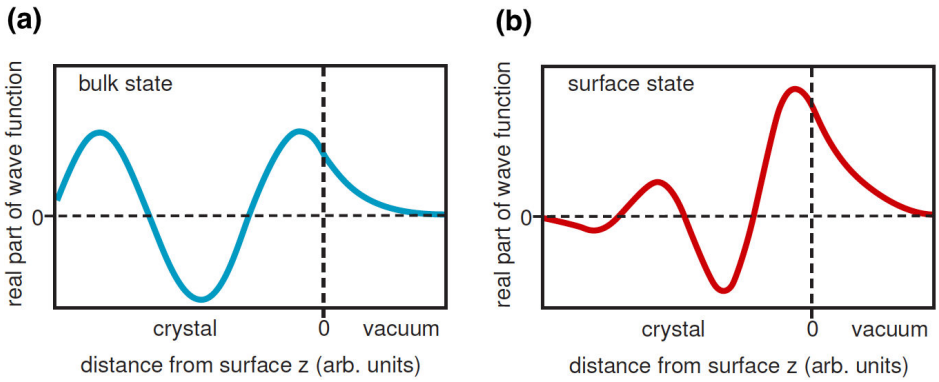

Figure 2.2: *Electron states in a crystal.* (a) Bulk state; periodical oscillation in the bulk and exponential decay in vacuum. (b) Surface state; oscillating in the bulk with an exponential modulation, matched with an exponential decay into vacuum. Figure reprinted from Ref. [25].

In the description of the bulk states, it was assumed without mention that $\boldsymbol{k}$ was a *real* vector, which made the wavefunctions mere oscillating functions. This was done because if $\boldsymbol{k}$ was complex, the Bloch waves would not *only* be oscillating, but also have an exponential part stretching towards infinity. Such solutions needed previously be discarded as non-physical, as the wavefunction would not be normalizable. However, after introducing a material surface, such solutions may yet be possible. If a Bloch wave where to be exponentially increasing in the direction where it is to be matched with the decaying form imposed from the vacuum, the resulting wavefunction will not grow towards infinity, and thus the wavefunction can be normalised. Assuming the presence of a surface only in the

[5] The form of this decay follows from the solutions for a free electron. A complete derivation of these are found in Ref. [22].

z-direction, that is, a crystal stretching infinitely in the xy-plane, the restriction of a real valued $\boldsymbol{k}$-vector is only lifted for the z-component. The wavefunction, ψ, now take the form

$$\psi_{\boldsymbol{k}_\parallel}(\boldsymbol{r}) = u_{\boldsymbol{k}_\parallel}(\boldsymbol{r}_\parallel)e^{-i\boldsymbol{k}_\parallel\cdot\boldsymbol{r}_\parallel}e^{-i\kappa z} \tag{2.4}$$

inside the crystal, and should be appropriately matched to the vacuum at the surface. Here, $\boldsymbol{k}_\parallel = (k_x, k_y)$ is a real vector, $\boldsymbol{r}_\parallel = (x, y)$ and κ is the complex wave vector in z-direction. The wavefunction becomes an oscillating wave, modified with an exponential growth towards the surface, and then matched to an exponential decay outside the material [25]. The resulting form is illustrated in Figure 2.2b. It is clear that such a state is highly localised at the surface and will therefore act two-dimensional. The surface state will not have any k_z dependence, as this quantity is meaningless for a two-dimensional state. An important quality about the surface states, is that they cannot be degenerate with any bulk states in the material. To avoid degeneracy, this surface state cannot overlap with any of the bulk states already present. More precisely, a surface state needs to appear in a band gap within the band projection on $k_\parallel$ [25].

2.4 Delta doping

Impurities and imperfections in a semiconductor can drastically change the electrical properties of the material. By deliberately adding impurities, a process known as *doping*, this can be exploited to modify and create desired behaviour of the material [29].

Consider the effect of impurities in silicon, which has four valence electrons. Each atom forms four covalent bonds, one with each of its nearest neighbours. Imagine one of the silicon atoms replaced by a phosphorus atom, which has five valence electrons. After the four covalent bonds are formed to each of the nearest neighbours, there will still be one electron left from the phosphorus. This electron is not strongly bound, and may be moved with relatively little energy up to the conduction band. The impurities, known as *donors*, have created extra energy levels in the material, located closely beneath the conduction band. The Fermi level[6] will effectively be shifted upwards, to reside about halfway between the donor level and the conduction band. As this process has the effect of adding

[6]The Fermi level is a hypothetical energy level of an electron, such that at thermodynamic equilibrium this level would have a 50% probability of being occupied. *The term "Fermi level" should be regarded as nothing more than a synonym for "chemical potential," in the context of semiconductors.* - N. Ashcroft, D. Mermin [2].

charge carriers to the system, it is known as *n-doping* the material. The opposite effect would be achieved by adding an impurity with three valence electrons and is called *p-doping*. This would in turn create an extra energy level with vacant holes, lowering of the Fermi level [35]. A schematic illustration of these situations is shown in Figure 2.3.

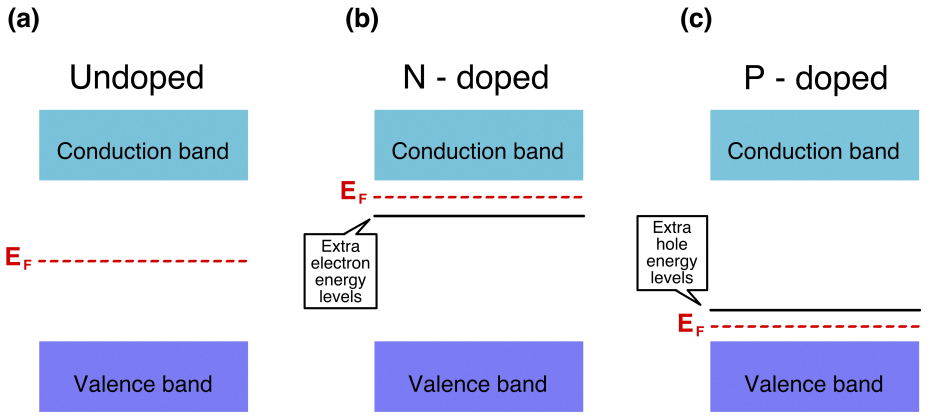

Figure 2.3: *Doping a semiconductor.* (a) Undoped system: Fermi level is determined by the energy that separates the occupied and unoccupied states. (b) Donor impurities have the effect of adding electrons to the system and raising the Fermi level. (c) Removing electrons will shift the Fermi level down.

The process of δ-doping is to create a high-density doping profile within a narrow, well-defined region in a semiconductor. Such a situation is illustrated in Figure 2.4, where the dopants, shown as dark circles in the inset of the figure, are confined to a single atomic plane. This confinement describes an ideal δ-layer, where in reality, the dopants will most likely be the subject of some redistribution and spread to the neighbouring planes. Still, as long as the dopants are confined within a layer less that 2.5 nm thick, the profile is consid-

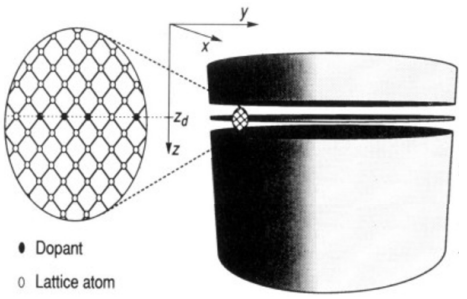

Figure 2.4: *δ-doped semiconductor.* Dopants in the material are restricted to one atomic plane. Illustration is based on Figure 1.1 from Ref. [45].

ered to be δ-function-like [45]. In
the previous section, both bulk- and surface states have been discussed. The effect of δ-doping may be of "trapping" bulk states, giving rise to other electronic states of fundamental interest, known as *quantum well states*.

2.5 Quantum well states

Consider the situation shown in Figure 2.5a. The illustration is that of a semiconductor; an empty conduction band with the Fermi level in the band gap underneath. The valence band is not shown. A n-type δ-layer is introduced, lifting the Fermi level (or more precise, the chemical potential) in this region. In thermodynamic equilibrium, the chemical potential is constant throughout the material, so this situation is clearly unstable. Donor electrons will flow from the dopant region, leaving behind positively charged ions.

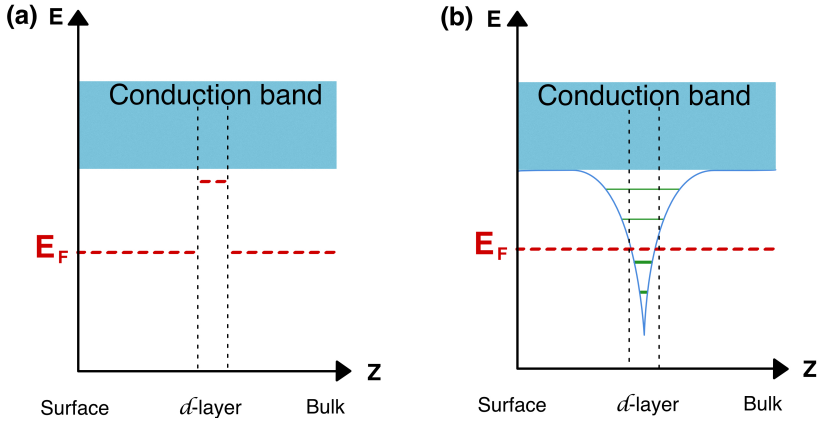

Figure 2.5: *Band bending effect from δ-doping.* (a) The Fermi level in the n-doped region of the δ-layer is lifted compared to the undoped region. This situation is not in chemical equilibrium. Donor electrons will flow from this region, creating an electric field. (b) The resulting situation manifests itself as a band bending in the dopant region, creating the possibility of quantum well states.

The situation will stabilize when the Fermi level is constant, now with an electric field in the direction normal to the δ-layer [25]. The effect of this manifests itself in the band structure as a *bending* of the bands in the dopant area. If the doping profile is strong and narrow enough, this can result in such an extreme bending as

to make the band dip beneath the Fermi level, resulting in the situation shown in Figure 2.5b. The wavefunction for such states will have an exponential decay in both directions perpendicular to the δ-layer, and the electrons will thus be highly localized to the dopant plane. We say that they are "trapped" in a potential well. In the bulk bands, the allowed states lie so close to each other in values of energy as to form a continuum. In the quantum well, however (being narrow and deep enough), the solutions become separated, allowing only discrete energy states. The four green lines in Figure 2.5 indicate such states, where the bottom two are below the Fermi level. The electrons filling these states are still free to move in the direction parallel to the doping region, but are now confined in the perpendicular direction. Such states are often described as a two-dimensional electron gas (2DEG), as their motion is confined to a two-dimensional sheet [25].

It can be difficult to separate quantum well states from the surface states discussed previously, but there is a distinct difference between the two. For the surface states, new solutions to the Schrödinger equation are possible by the existence of a surface on one side (since the wavefunction is allowed to exponentially increase in the direction where it is to be matched to the vacuum). The quantum well states, however, are not new solutions arising from a complex component of the wavevector. They are merely bulk states that are confined to the dopant region by a strong band bending [25]. Because of this, we can expect that the behaviour of the quantum well states will be somewhat influenced by that of the bulk states from which they are derived, a point which will be discussed in later chapters.

Chapter 3

Photoemission Techniques

The electrons in a material do not move independently from each other or their surroundings, but their movements are a result of the net interactions of the whole system. In this way, an electron carries information not only about itself, but also regarding the material of its residence. Several characterisation techniques are founded on this concept. The main idea is to extract electrons from the material of interest, detect characteristics of these electrons, and in this way gain information about the material itself.

The purpose of this section is to provide a basic explanation of the main principles regarding Photoemission Spectroscopy (PES), and the refinement, Angle-Resolved Photoemission Spectroscopy (ARPES). The latter of these is the technique used in this work. For a more thorough description of the variety of phenomena regarding photoemission, it is referred to the solid state physics textbooks [27, 29, 56].

3.1 Three-Step Model

The three-step model describes the photoemission process in the following steps: (i) A photon excites an electron; (ii) the electron travels through the crystal to the sample surface; (iii) the electron transmits through the surface and escapes into vacuum.

The three-step model provides a somewhat artificial description of the photoexcitation, as the whole process in reality should be treated as one step. Nevertheless,

the model is commonly used, as it is conceptually simple and the theory provides results that are not very different from the complex one-step model [27]. In the following, a description of the different steps will be presented. Some key notions, to give a better perception of the photoemission process, will also accompany the description.

3.1.1 Step 1: Excitation of the electron

The first step describes the local absorption of a photon which results in the excitation of an electron. The electron absorbs the photon energy $h\nu$, and is lifted to a higher energy state [56]. Depending on the electron initial and final state, different properties of the specie is probed, and different techniques are adapted. The excitation process of XPS and ARPES is illustrated in Figure 3.1.

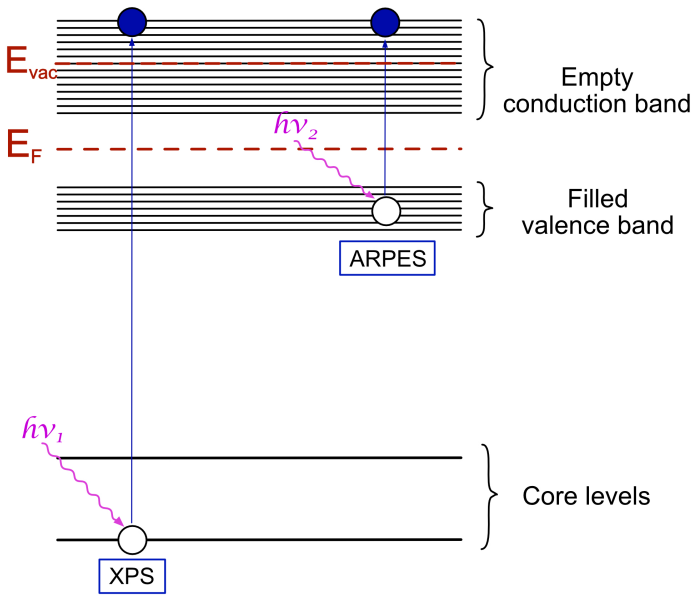

Figure 3.1: *Excitation of an electron.* First step in the photoemission process as described by the three-step model. An electron is, by photoelectric absorption, excited from an initial to a final electron state. Figure is re-adapted from Ref. [53].

Simple as this may seem, something in this situation is not obvious. In order to be freed from the sample, the electron must be lifted to an energy state above the vacuum level. However, the electron cannot be excited to any given final state. It needs an available, existing state that is resulting from the material band structure to be excited into. It might seem strange that the material will have states above the vacuum level at all, as one may consider this to be outside the sample. Looking back at the band structure in Figure 2.1c, however, it is clear that solutions will exist for, in principle, infinite energy values. The vacuum level is typically a few eV higher than the Fermi level. In Figure 3.1 it is drawn to lie in the conduction band (although this is not always the case), illustrating that solutions to the Schödinger equation do not cease to exist by crossing the vacuum level.

3.1.2 Step 2: Propagation to the surface

Having been excited into a final state which lies above the vacuum level, the electron is now free to move and is propagating through the material to the surface. We view the electron as following a path of constant potential, so that the energy is conserved during the travel. However, not all electrons are so lucky as to propagate to the surface without undergoing any inelastic scattering and losing some of their energy. This effect manifests itself in the measurements by a "tail" of electrons with kinetic energy less than the main signal [57]. At first glance this may seem like a highly inconvenient disturbance, but an adept experimentalist may be able to extract useful and interesting information from the behaviour of these tails.

It is now straightforward to realise that photoemission should be a surface sensitive technique. The incoming photons will penetrate in the scale of microns into the sample, but electrons that get excited from the deeper layers of the material will have a longer travel towards the surface. Such electrons thus have a higher probability of getting inelastically scattered along the way. The average length an electron travel before such scattering is known as the *inelastic mean free path*, λ, and is a characteristic of the material and the electron kinetic energy. By studying a large number of materials under a wide range of kinetic energies, λ is found to be highly dependent on the electron kinetic energy and lesser dependent on the specific material [26]. This resulted in what is known as the *universal curve*, shown in Figure 3.2, which is frequently used for estimating the inelastic mean free path of the traveling electrons [47].

Usually, one defines the *sampling depth*, d, as the depth for which 95 % of the electrons arise within. This is given by

$$d = 3\lambda_e \cos\theta \tag{3.1}$$

where λ_e is the electron inelastic mean free path and $\cos\theta$ is a factor accounting for the increased length the electrons have to travel if the sample is tilted relative to the photoelectron analyser [26]. When detecting electrons with a kinetic energy of $E_K = 200$ eV at normal emission, it is understood from Figure 3.2, and by the use of Eqn. 3.1, that we are probing roughly 2 nm into the sample.

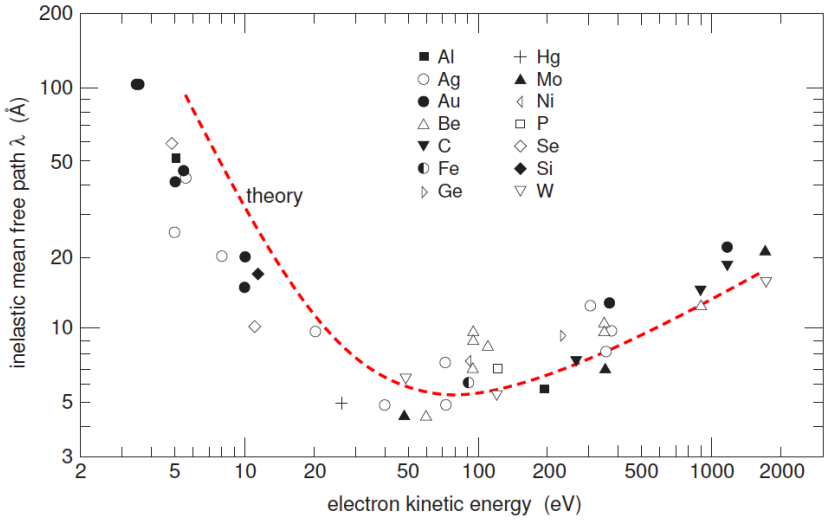

Figure 3.2: *Universal curve of inelastic mean free path.* The curve shows the calculated (red dashed line) and experimentally obtained (black and white symbols) values for the inelastic mean free path of electrons in a solid. Figure reprinted from Ref. [47].

3.1.3 Step 3: Transmission through the surface

The last step in the model considers the transmission of the electron through the surface potential barrier. This process is described by a probability factor, which is obtained by matching the bulk Bloch eigenstates inside the material to free-electron plane waves in vacuum [14].

Inside a material, the electron may exchange momentum with the crystal lattice. The lattice carries momentum in the quanta of $\mathbf{G}$, determined by the lattice periodicity. Since the wavefunction is periodic with this quantity, such an exchange

will not alter the electron description. As the electron leaves the sample, however, the symmetry in the direction normal to the surface is broken, and any amount of momentum $\boldsymbol{k}_\perp$ may be exchanged. That is, given that the translational symmetry of the surface potential is conserved across the surface boundary, the parallel component of the electron momentum must be conserved under the transmission, but the same is *not* true for the perpendicular momentum [12].

3.2 Photoemission Spectroscopy

Having established the important details of the three-step model of photoemission, we now turn to consider how this might be used to extract information about a sample of interest. The relation between a photon of energy $h\nu$ and the outgoing electron with kinetic energy E'_K, is simply described from conservation of energy as

$$h\nu = E'_K + E_B + \phi_S. \tag{3.2}$$

Here, E_B is the energy of the electron initial state, measured relative to the Fermi level and ϕ_S is the energy needed to extract the electron from the sample Fermi level and out to vacuum. These are known as the *binding energy* and the sample *work function* respectively. From vacuum, the electrons may be collected by a suitable lens system, and thereby analysed using a photoelectron energy analyser. It is important to remember that the analyser has a work function, ϕ_A, of its own. By electrical connection between the sample and the analyser, the Fermi level in these materials will align, and the electrical potential between them becomes $\phi_S - \phi_A$. We then realise that the relation between the kinetic energy of the electron leaving the sample and the kinetic energy upon entering the analyser, E_K, becomes

$$E'_K + \phi_S = E_K + \phi_A, \tag{3.3}$$

as illustrated in Figure 3.3. Combining Eqn. 3.2 and 3.3, the expression to correctly extract the binding energy becomes

$$E_B = h\nu - E_K - \phi_A. \tag{3.4}$$

Note that the sample work function cancel, but the analyser work function must be known [13]. By exposing the sample of photons carrying a specific energy, and measuring E_K, it is possible to determine the electron binding energy.

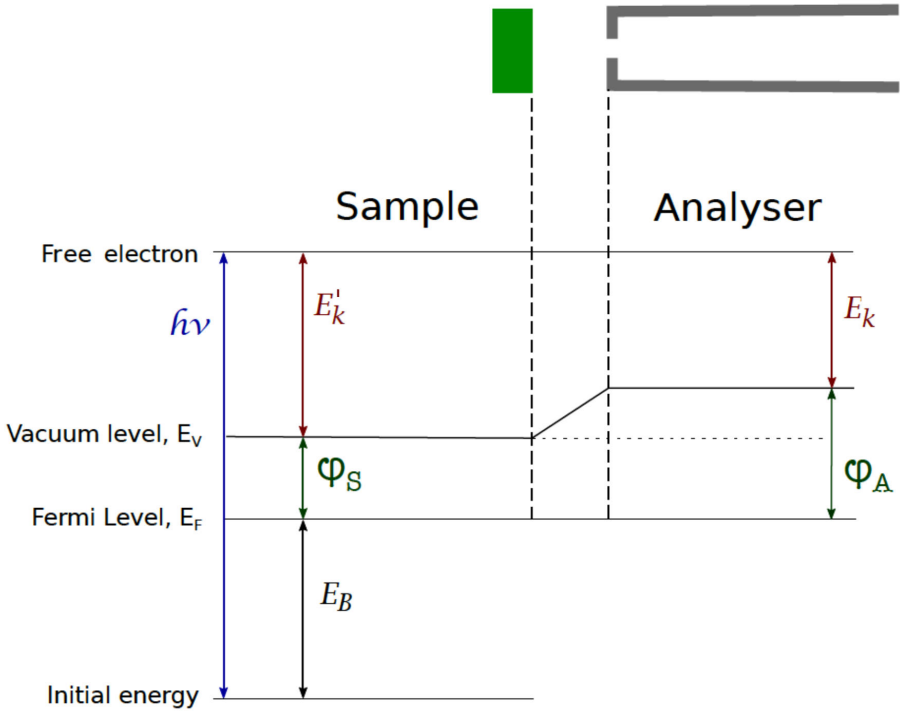

Figure 3.3: *Kinematics of a photoemission experiment.* Illustrating the relation between different variables in the photoemission process. The binding energy, E_B, is calculated by knowing the analyser work function, ϕ_A, measuring the kinetic energy, E_K, and controlling the photon energy, hv.

3.3 Angle-Resolved Photoemission Spectroscopy

With technological progress, a refinement of the photoemission technique, known as angle-resolved photoemission spectroscopy, became possible. Here, not only the kinetic energy, E_K, is measured, but also the wavevector $\boldsymbol{K}$ *in vacuum* is obtained. The wavevector is a measure of the momentum carried by the electron, related by $\boldsymbol{K} = \frac{1}{\hbar}\boldsymbol{P}$. This is used to extract information about the wavevector carried by the electron traveling *inside* the crystal, $\boldsymbol{k}$, and thus obtaining detailed information about the band dispersion and Fermi surface of the sample. For simplicity, $\boldsymbol{k}$ is often just referred to as the electron momentum. A schematic of an ARPES measurement is shown in Figure 3.4, where both $\boldsymbol{K}$ and E_K are measured.

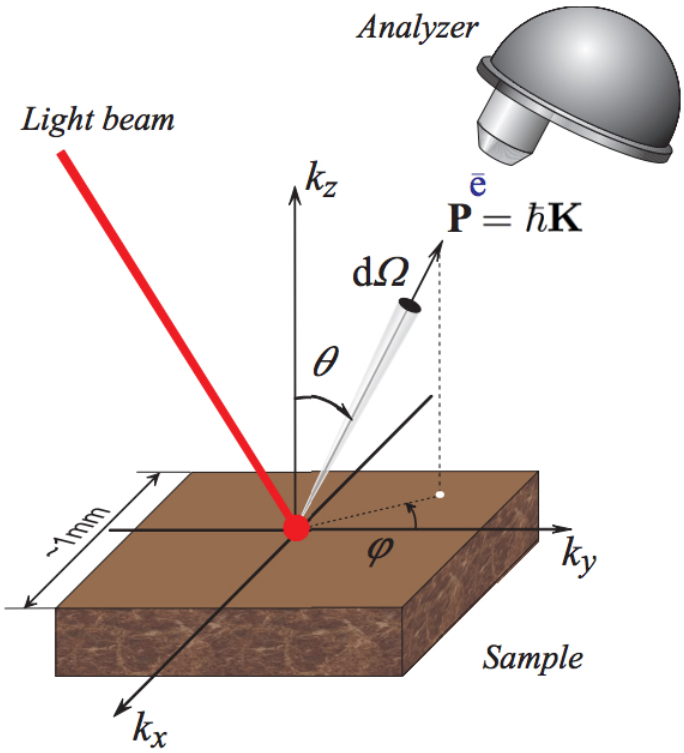

Figure 3.4: *Geometry of an ARPES experiment.* Electrons are freed from the material by an incoming light beam. They leave the sample in an angle described by the parameters θ and ϕ. Figure reprinted from Ref. [61].

The magnitude of the electron momentum in vacuum is given by $\boldsymbol{K} = \frac{1}{\hbar}\sqrt{2mE_K}$ and from the geometry of the experiment its components become

$$\boldsymbol{K_x} = \frac{1}{\hbar}\sqrt{2mE_K}\sin\theta\cos\phi, \tag{3.5}$$

$$\boldsymbol{K_y} = \frac{1}{\hbar}\sqrt{2mE_K}\sin\theta\sin\phi, \tag{3.6}$$

$$\boldsymbol{K_z} = \frac{1}{\hbar}\sqrt{2mE_K}\cos\theta. \tag{3.7}$$

The extraction of the electron momentum inside the solid is based on the principle that, under photoemission, the emitted electron does not undergo a shift in momentum parallel to the sample surface, so that

$$\boldsymbol{k}_{\parallel} = \boldsymbol{K}_{\parallel}. \tag{3.8}$$

The reason for this is that the absorbed photon carries so little momentum as to assume that $\boldsymbol{k}_{photon} \approx 0$, and the parallel momentum is not affected by transmission through the surface[1]. With a sample orientation as illustrated in Figure 3.4, and by combining Eqn. 3.5 and 3.6, the parallel component may be expressed in terms of measurable quantities by

$$|\boldsymbol{k}_{\parallel}| = \sqrt{k_x^2 + k_y^2} = \frac{1}{\hbar}\sqrt{2mE_K}\sin\theta. \tag{3.9}$$

However, the wavevector perpendicular to the surface, $\boldsymbol{k}_{\perp}$, is not conserved. Still, it is possible to determine the value of $\boldsymbol{k}_{\perp}$, by making an *a priori* assumption of the dispersion of the bulk final states. To this end, we assume the final states have a parabolic dispersion, and can then be described as

$$E_f(\boldsymbol{k}) = \frac{\hbar^2\boldsymbol{k}^2}{2m} - |E_0| = \frac{\hbar^2(\boldsymbol{k_{\parallel}^2} + \boldsymbol{k_{\perp}^2})}{2m} - |E_0|. \tag{3.10}$$

Here, the value of $|E_0|$ corresponds to the bottom of the valence band as indicated in Figure 3.5, which illustrates the kinematics of a photoemission process. It follows further from this illustration that the bulk final state energy may be

[1]The assumption $\boldsymbol{k}_{photon} \approx 0$ is not reasonable for high photon energy ARPES measurements, and a correction to Eqn 3.9 and Eqn. 3.11 is required. The corrections at normal emission are given by $k_{\parallel} = \frac{1}{\hbar}\sqrt{2mE_K}\sin\theta - \frac{2\pi\nu}{c}\cos\alpha$ and $k_{\perp} = \frac{1}{\hbar}\sqrt{2m(E_K\cos^2\theta + V_0)} + \frac{2\pi\nu}{c}\sin\alpha$; this has been applied to the results in Chapter 6, where a higher photon energy is used.

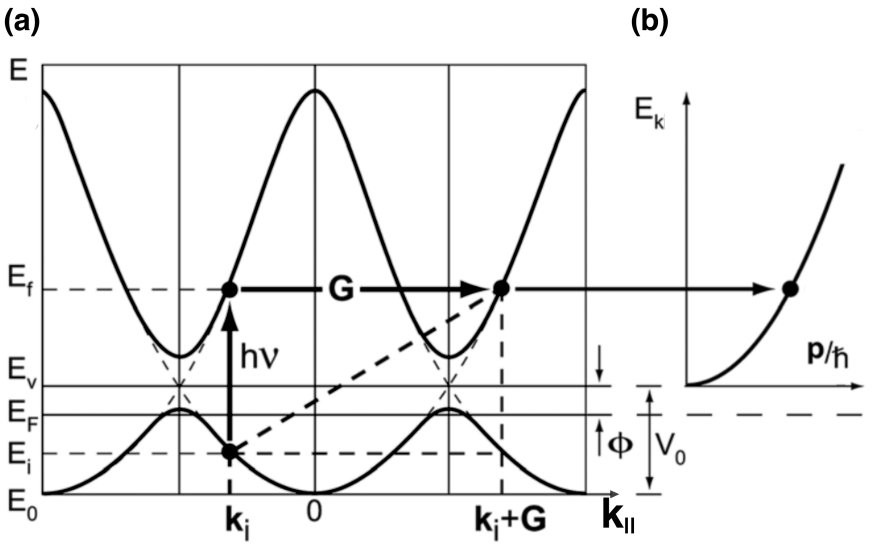

Figure 3.5: *Kinematics of an ARPES experiment.* Developed from the three-step nearly free electron final state model. (a) Direct transition in the solid. (b) Free electron final state in vacuum. Schematics based on Figure 4 in [14].

expressed as $E_f = E_K + \phi$. Combining this with Eqn. 3.9, the perpendicular component of the electron momentum may be expressed as

$$|\boldsymbol{k}_\perp| = \frac{1}{\hbar}\sqrt{2m(E_K \cos^2\theta + V_0)}. \tag{3.11}$$

The value $V_0 = |E_0| + \phi$ is known as the *inner potential* of the sample, and describes the energy at the bottom of the valence band referenced to the vacuum level, E_V. Note that in the above context, E_K is also referenced to the vacuum level, while both E_0 and E_f is referenced to the Fermi energy, E_F.

We now understand that this technique allows a detailed description of the dispersion relation $E(\boldsymbol{k})$ of our sample, simply by measuring the kinetic energy and the emission angle. The only parameter left to determine, is the inner potential, V_0, which can be extracted from the measured periodicity of the dispersion $E(k_\perp)$. Various methods also exists for calculating the inner potential in crystals [52], and a great many determined values are now available in the literature.

3.4 Mapping of 2D and 3D states

In Chapter 2, the characteristics of different electronic states were discussed. Some states were shown to have a wavefunction highly localized to a single atom layer (*e.g.* in the xy-plane), thereby named 2D states. Such a state is confined in the z-direction and will therefore not inhibit any k_z dependence. If we still were to use the *a priori* assumption of Eqn. 3.10 to describe these electrons (as is the case), we are assuming that the energy is depending on a quantity that it is, in fact, independent from. The result is, by plotting the energy (or $k_{\parallel}$) as a function of k_z, the 2D states will appear to be constant, while the 3D states will vary. This is therefore a simple and elegant way of differentiating such states.

It can be a challenge to separate different 2D states from each other (*e.g.* surface states from quantum well states), and one sometimes need settle with mere indications. Surface states will, as mentioned, appear in the projected band gap. Any 2D state appearing outside this region will then clearly not be associated with a surface state. For 2D states appearing in the band gap however, the opposite argument is not valid. It is therefore important to have complete knowledge of the band structure before inducing a δ-layer to the sample, so one can associate the δ-layer with any eventual new states appearing in the measurements.

It may be questioned how a 2D state can be detected in photoemission at all, carrying no k_z momentum. Even if such an electron were to get excited, and instantaneously appear outside the sample (as within the one-step-model), it should never reach the detector. Strangely, such states *are* frequently detected. Where then, do this additional momentum arise? The answer is that it comes from the lattice itself, which carries momentum in the form of lattice vibrations. This momentum exists in quantities of $\boldsymbol{G}$, and can be transferred to the electron. We need not worry that such a transition may obscure the $k_{\parallel}$ mapping, as this would just change the momentum by a repeating period. This is illustrated in Figure 3.5, showing that a vertical transition between the initial and final bulk states is equivalent to a transition with the reciprocal lattice vector, $\boldsymbol{G}$, added to the momentum vector[2].

[2] *"in a nearly-free electron gas, optical absorption may be viewed as a two-step process. The absorption of the photon provides the electron with the additional energy it needs to get to the excited state. The crystal potential imparts to the electron the additional momentum it needs to reach the excited state. This momentum comes in multiples of the reciprocal-lattice vectors G: So in a reduced zone picture, the transitions are vertical in wave-vector space. But in photoemission, it is more useful to think in an extended-zone scheme."* - G.D. Mahan [32].

Chapter 4

Experimental Requirements and Methods

An important consideration for any experiment is the apparatus involved, as this often dictates both the possibilities and restrictions imposed on the experimentalist. The measurements presented in this thesis are obtained at three different synchrotrons. An introduction to the general concepts of a synchrotron facility will therefore be presented first, followed by the description of fundamental equipments and the experimental methods used.

4.1 Synchrotron facility

In order to conduct a photoemission experiment one will need a source of photons. This can be provided by the acceleration of charged particles, which causes emission of electromagnetic radiation [30]. The electromagnetic radiation emitted when charged relativistic particles are being deflected is called *synchrotron radiation*. In a synchrotron facility, this type of radiation is produced artificially.

4.1.1 Synchrotron radiation

The electrons used to produce radiation are maintained circulating in a storage ring at near-light speed and at almost constant energy. When thinking about the

size and speed of the particles involved, one realise that this is not an effortless accomplishment. The electron trajectories are affected by everything in the ring. in addition, they naturally repel each other. Therefore, their trajectories need to be constantly corrected to prevent them from crashing into the sides of the storage ring. The electrons are kept circulating in different "bunches" inside the ring. Each bunch will quickly spread out, so timed electric fields are switched on and off to assemble the bunches [50]. Some electrons will unavoidably crash into the walls, so there is need for a "top up" of electrons from time to time. The circumference of a synchrotron storage ring is highly variable, ranging from some meters to a few kilometers. The choice of circumference influences the accessible photon energy range of a synchrotron facility.

Since the electrons are kept in circulation (and therefore are accelerating), they produce radiation constantly. However, these photons are of lower energy than those desired for most experiments. To make the electrons produce the desired radiation, devices such as *wigglers* and *undulators* are placed along the ring. These are magnetic devices which impose a force, known as the Lorentz force, on the electrons, causing their trajectory to bend in a controlled manner. [21]. An illustration of a wiggler device is shown in Figure 4.1. Here, a series of magnets are placed with alternating poles, causing the electrons traveling through this field to "wiggle" sideways and produce an intense and narrow beam of electromagnetic radiation. The magnets are constructed in such a way that the radiation emitted by a given electron at one oscillation is in phase with the radiation from the following oscillations. The undulator works according to the same principle, but has device parameters resulting in a narrow energy spectrum in the produced radiation.

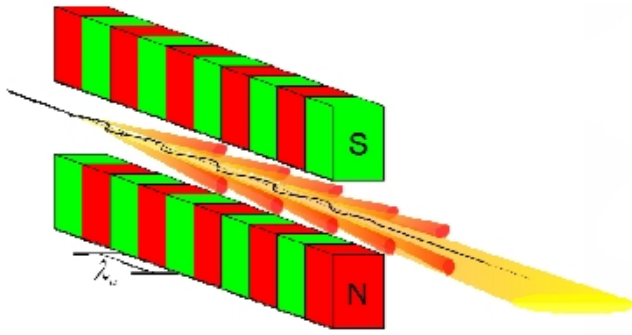

Figure 4.1: *Insertion device in storage ring; wiggler.* The device creates an alternating magnetic field that causes the passing electrons to oscillate and produce electromagnetic radiation. Reprinted from Ref. [19].

4.1.2 Synchrotron beamline

The radiation beam produced in the storage ring must be guided to the experiment end-station. This is accomplished with a *beamline* that consists of a series of mirrors that focus the beam onto a monochromator. The monochromator allows a fine selection of the photon energy by spatially separating the frequencies of the radiation, and filtering out all but a narrow frequency range of the radiation. The monochromatic beam is focused into the end-station and ready for experimental use. An illustration of a beamline and an overview of a synchrotron are presented in Figure 4.2.

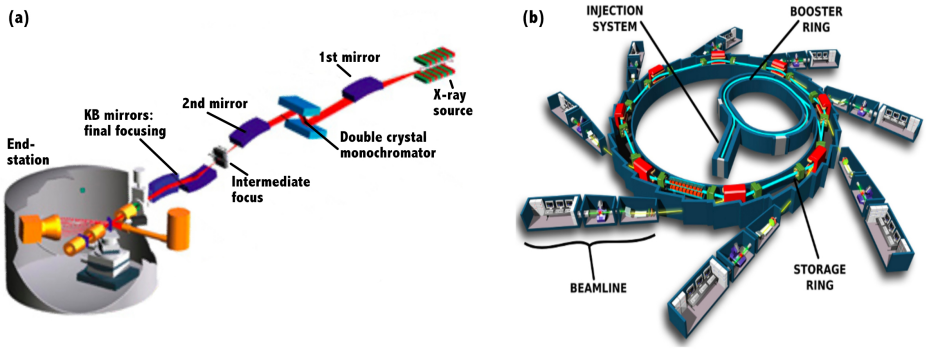

Figure 4.2: *Synchrotron beamline and overview.* (a) Detailes of the SUL-X beamline at the ANKA test facility in Leopoldshafen, Germany [28]. (b) Overview of the SOLEIL synchrotron in Paris, France [10]. Radiation is produced in the storage ring and guided to the end station through the beamline.

The effort, knowledge, and expenses required to develop and maintain a synchrotron is immense, which is why there must be good reasons for building such a facility. Perhaps the most attractive feature offered by a synchrotron is the ability to tune the photon energy reaching the sample, which may be done by changing the gap of the wiggler/undulator or the positioning of the monochromator [1]. Simpler sources of electromagnetic radiation may provide photons at several discrete energies, but to have a continuously tuneable beam of radiation offers a huge advantage in several experimental techniques, including, as will be shown in the following chapters, ARPES. The radiation produced in a synchrotron is also of high intensity, making it possible to perform the experiments fast. This is beneficial since the experimentalist often works against the clock, as samples may have a limited lifetime before they get contaminated.

4.2 Analyser and Detector

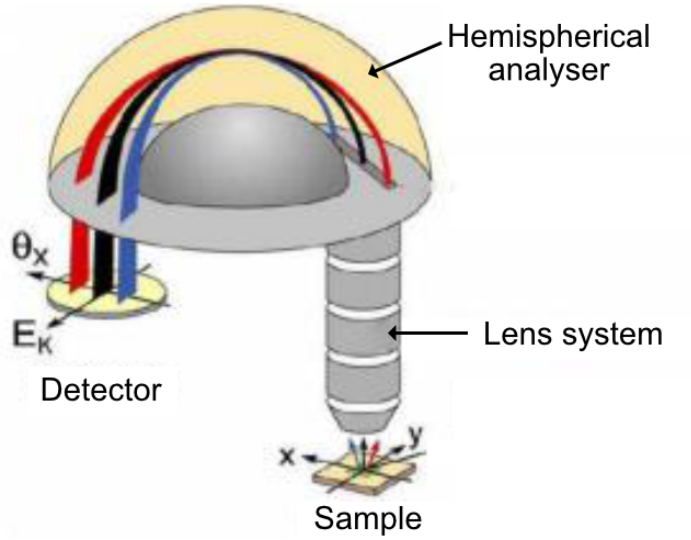

Figure 4.3: *Hemispherical electron analyser.* Schematics showing the operating principle of an hemispherical electron analyser. Photoelectron intensity is mapped with respect to both the electron kinetic energy and the emission angle θ. Reprinted from Ref. [54].

There are several different ways to analyse the photoelectrons ejected by the synchrotron radiation. In the experiments presented in this thesis, this was accomplished using a hemispherical electron analyser. Such an analyser consists of two metallic hemispheres, with a potential difference applied between them. The potential difference creates equipotential surfaces between the hemispheres, affecting the electron trajectories. This work as an energy filter, only allowing electrons within a certain kinetic energy range to reach the detector screen, while the rest will hit the hemisphere walls. Before reaching the analyser, the electrons are collected by a suitable electrostatic lens system. The lens system allows a retardation of the electrons, making it possible to select which kinetic energy range is allowed to reach the detector. A schematic of the hemispherical electron analyser is presented in Figure 4.3. The design preserves the electrons' angular trajectory along one direction. By using a 2D detector it is therefore possible to map the photoelectron intensity with respect to both the kinetic energy and the emission angle θ, which again can be converted to $\boldsymbol{k}$.

4.3 Ultra high vacuum

When conducting a surface science or photoemission experiment, there is often a need to perform the experiment in a clean environment. Ideally, this would be to measure the sample with not a single contaminant stuck on the surface or floating in the surroundings to disturb the measurements. One strives towards this situation by taking great care in preparing the samples and keeping the surroundings at very low pressure during all measurements.

To get an impression of the pressure required, it is insightful to do a rough estimate over the number of O_2 molecules that hit a surface of 1 cm^2 per unit time if the pressure is $P = 10^{-6}$ mbar. Kinetic theory of gases gives the *impingement rate*, Γ, as

$$\Gamma = \frac{P}{\sqrt{2\pi M k_B T}}. \tag{4.1}$$

Here, M is the molecular mass, k_B is the Boltzmann constant and T is the temperature. At room temperature, this results in an impingement rate for O_2 at $\Gamma = 3{,}8 \cdot 10^{14}$ $cm^{-2}s^{-1}$. The average number of molecules on a 1 cm^2 surface area is in the order of $\sim 10^{15}$. This means that, with the aforementioned pressure, it will take about 3 seconds to contaminate the entire sample surface. This clearly illustrates the need for much lower pressure values. Usually, one requires the pressure to be in the order of 10^{-9} mbar or below; a condition categorised as ultra high vacuum (UHV) [33].

This ultra high vacuum is obtained and maintained by an intricate system of different pumps and chambers, that can be sealed off from each other upon transferring the sample in and out of the measurement system. The significance of a successfully prepared sample is obvious, as the process of changing a ruined sample may cost a day of experiment time.

4.4 Sample preparation

An important step in preparing a photoemission experiment is to ensure a clean sample. There are several common methods for cleaning a sample before transporting it into UHV. Some materials, such as metals with a weak out-of-plane bonding, are well suited for *cleaving*, the process of tearing off the top atom layers. Silicon is not suited for cleaving, but the standardised cleaning procedure of Radio Corporation of America, involving different chemical processes as described in Ref. [59] is usually followed. Nevertheless, during the transportation into the system, the sample is exposed to atmosphere, and thus gets contaminated by

molecules in the air. Due to the short mean free path of photoelectrons, a large fraction of the measured intensity arises from the surface, making it important for this to be clean. Contaminants will also increase the scattering of photoelectrons and may even dramatically alter the electronic properties of the sample [5]. It is therefore vital to clean the sample even after it is brought under UHV conditions. In the work of this thesis, the *in situ* cleaning of samples was accomplished by the processes of *annealing* and *flashing*. *In situ* sample growth has also been conducted. This was done using two different methods, namely *gas dosing* and *thermal evaporation*. These will be discussed in the following sections.

4.4.1 Annealing and flashing

In the process known as *annealing*, thermal energy is applied to the system, with the aim to overcome the desorption energy of the contaminant species. The material must be heated sufficiently to allow free movement of the particles, and is usually held at this temperature for several hours in order to let particles migrate from within the sample. One can also heat the sample to as high a temperature as possible for a few seconds, known as *flashing* the sample. This is an effective way of getting rid of an oxide layer and other contaminants that eventually will form on the surface of the sample, even under UHV conditions [25]. Both annealing and flashing are generally done by one or both of two different methods, known as *direct heating* and *indirect heating*. These are illustrated in Figure 4.4. Direct heating is achieved by applying a current through the sample, created by an applied voltage. The process is only limited by the sample resistance, thereby working poorly for insulators. During indirect heating, a current is sent through a filament to make it hot. The filament is placed close to the sample, which gets heated by thermal irradiation [33].

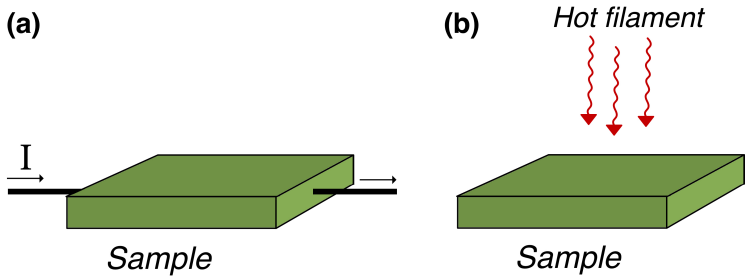

Figure 4.4: (a) *Direct heating*; the sample is heated by passing a current through it. (b) *Indirect heating*; the sample is heated by thermal irradiation from a hot filament.

4.4.2 Gas dosing

Gas can be used to coat a material through a process whereby the gas reacts chemically near or on a substrate to form a solid product. In the work of this thesis, phosphine gas, PH_3, was used to create δ-layers of phosphorus on a silicon substrate. This was achieved by introducing phosphine gas to the chamber containing the sample, and letting the sample surface saturate with the gas molecules. To subsequently remove the H atoms, the sample was under a short anneal. A temperature of 350°C for 10 seconds is shown to remove H atoms and incorporate P to the surface, producing a coverage of $\frac{1}{4}$ monolayer (ML) of phosphorus at the sample surface [44, 58]. The process of gas dosing and annealing is illustrated in Figure 4.5.

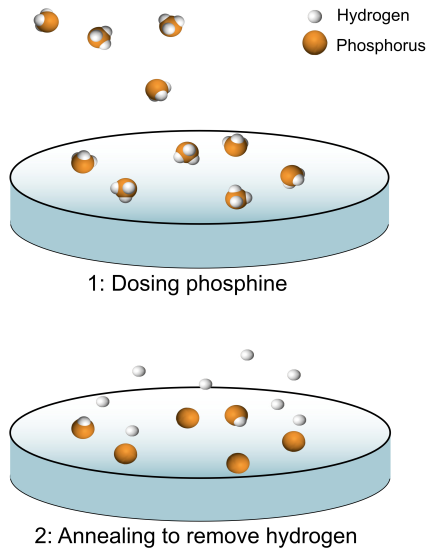

Figure 4.5: *Phosphine dosing and annealing.* Sample is dosed with PH_3 and subsequently annealed to remove H. Illustration based on Fig. 2.8 in Ref. [33].

After a coverage of phosphorus is prepared, the sample may be *capped* with silicon. That is, new silicon may be deposited on top of the phosphorus, creating a buried δ-layer. The capping layer was created by thermal evaporation of silicon.

4.4.3 Thermal evaporation

Thermal evaporation is one of the oldest techniques used for depositing thin film materials on a substrate in vacuum. The method is still widely used in laboratories, as it is simple, precise and versatile. The general principle is to heat the depositing material, making it evaporate, and then transport the vapour to the substrate and letting it condense to a solid film [46].

Heating the depositing material may be done both by the direct and the indirect method, similarly as to the process in Figure 4.4. In this work, thermal evaporation was conducted as part of the fabrication of Si:P δ-layers, where new silicon

was evaporated on top of the dopant layer, *capping* the sample. The evaporation was conducted with a homemade evaporator, based on the direct heating process. This is shown in Figure 4.6.

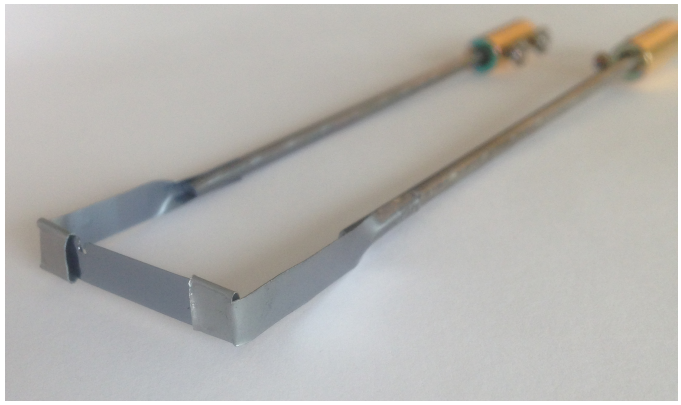

Figure 4.6: *Silicon evaporator.* A piece of silicon wafer is connected to the chamber in such a way that a current can flow through it. The temperature increases until silicon evaporates, covering the sample substrate.

A piece of silicon wafer was connected to the inside of the UHV chamber by rods and clips made of stainless steel. One can easily apply a voltage between these rods and make a current flow through the silicon wafer, heating it to the temperature of evaporation. The sample substrate was simply held in close vicinity to the wafer, thus getting covered by silicon vapour which condensed upon contact with the cool sample. After silicon deposition, a final step of annealing was conducted to recrystallise the capping layer surface.

4.5 Materials

Silicon and diamond may seem unrelated, but there exists several similarities between these materials. Silicon, with its nuclei accommodating 14 protons, is found just beneath diamond (hosting 6 protons) in the periodic table. This means that they both have four valence electrons. The orbital nature of these are also similar. For both materials, the valence electrons reside in s and p orbitals, and in order to create covalent bonds, the s orbital mixes with the three p orbitals to form what is known as the sp^3 hybridisation, shown in Figure 4.7.

This makes silicon and diamond crystallise in the same tetrahedral crystallographic structure, and as a result the band structure, presented in Figure 4.8, of the two materials is quite similar. The valence band maximum (VBM) appears at the high symmetry Γ point. This band splits in two going towards the high symmetry X or L point, while into three if moving in the Γ-K direction. The conduction band minimum (CBM) occurs for both materials near the high symmetry X-point, though somewhat closer to X in the case of silicon.

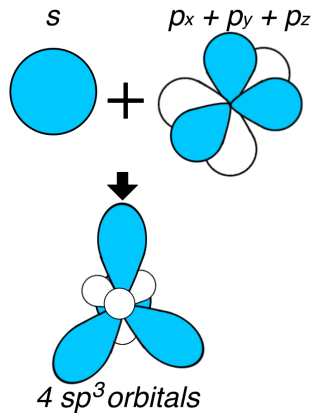

Figure 4.7: Illustration of the sp^3 hybridisation.

In the current work, the primary difference between the δ-doping conducted on these materials is the nature of the dopants used. The silicon dopant layer is produced by phosphorus, an n-donor, while the diamond epilayer is heavily boron-doped, making it p-type. An n-type doping has the effect of adding electrons to the system, raising the Fermi level, and in turn induces a downward band bending. For silicon, the conduction band minimum is therefore of special interest, occurring close to the high symmetry X-points. The situation for diamond is different, as the p-type doping lowers the Fermi level, making the Fermi contour appear at Γ. This means that for silicon, the focus of attention will be the conduction band minimum, while for diamond the valence band maximum is the point of highest interest.

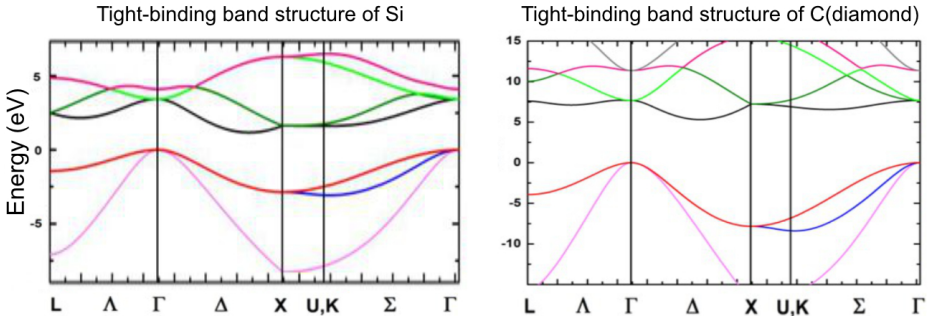

Figure 4.8: *Band structure.* Tight-binding calculations describing the band structure of Silicon and Diamond. Re-adapted from Ref. [40].

Chapter 5

Silicon δ-doping

In the previous chapters, the theory behind electronic band structure and concepts regarding photoemission have been presented. These have aimed to explain different electronic states in a crystal and the technique utilised for characterising these states, ARPES. Sample growth and methods for sample preparation have been introduced, in addition to some insight in the experimental environment associated with a synchrotron and an introduction to the investigated materials. Now we turn to the experimental findings. The results obtained will be presented in two parts. In this chapter, all results regarding the measuring of δ-layers in silicon is presented, while the next chapter is dedicated to the measurements of diamond thin- and thick film.

The work presented in this chapter investigates the quantum confinement effect in δ-doped silicon, by examining samples with phosphorus δ-layers varying from an atomically sharp doping profile to a 4.0 nm thick layer. In doing so, we hope to verify experimentally, for the first time, the existence of the 1Δ quantum well states which have been found in theoretical calculations. Before the results are presented, this chapter provides an introduction to the current findings within Si:P δ-layers, the approach used in the experiment, and a description of the measured samples.

5.1 Previous works

Investigating δ-layers in silicon has been a subject of growing interest the past few years. The theoretical band structure of phosphorus δ-layers in silicon has

been studied intensely by different methods such as tight-binding (TB), pseudopotential method (PP) and by density functional theory (DFT) [7, 8, 9, 31]. A predicted band structure of an ideal ordered Si:P δ-doped layer with the phosphorus covering $\frac{1}{4}$ monolayer at 4 K is shown in Figure 5.1, with the band structure of pure silicon with the same dimensions inset as dashed black lines as a comparison.

The calculations predict that the quantum well created from the δ-doped layer induces a strong confinement that pulls down the bands significantly. This confines electrons in dense impurity bands under the standard silicon conduction band, with a large splitting between the confined subbands. An increased doping density is found to increase the confinement and to lower the impurity band energies [31]. The first three subbands of this calculation are named 1Γ, 2Γ and 1Δ. They are interpreted to derive from the band projection of the bulk silicon valleys originating at the high symmetry X points. The quantum well states are confined to the dopant plane and thus act as 2D states. They will lose their k_z dependence and should therefore be fully described within the 2D Brillouin zone. This can be thought of as a compression of the 3D zone down to a plane as illustrated by Figure 5.2. Note that these states originate from the same high symmetry point in the 3D Brillouin zone, but their relative positions have changed in the projected picture. The out-of-plane valleys are now located at the 2D zone centre, while the in-plane valleys are projected to their own positions.

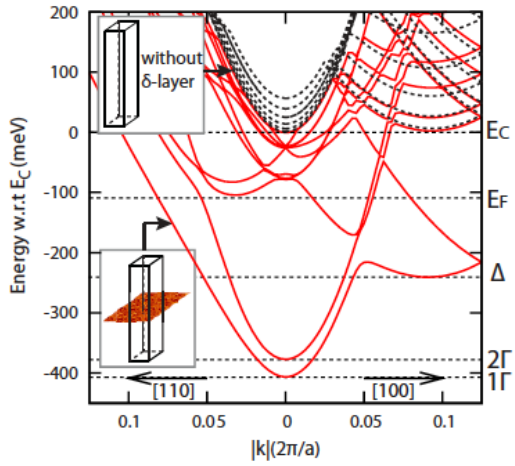

Figure 5.1: Calculated projected band structure for $\frac{1}{4}$ ML Si:P δ-doped layer (red) and for pure silicon (black dashed lines). Reprinted from Ref. [31].

Several experiments have been conducted with the goal of locating and characterising these states, which have led to the observation of both 1Γ and 2Γ [36, 39]. The experiments have revealed the Fermi level position, and thereby the occupancy, effective masses, and valley splitting of the 1Γ and 2Γ bands. The

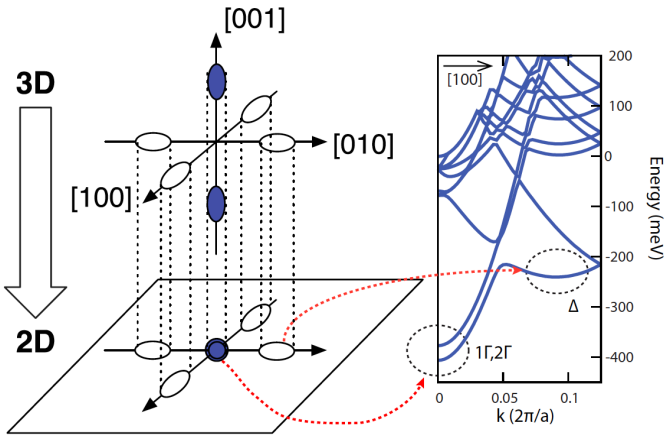

Figure 5.2: *Band projection diagram for the highly confined 2D δ-layers.* Two valleys (dark) are projected to the Γ point, and four valleys are projected to their own positions. Reprinted from Ref. [31].

understanding of these properties it essential for the use of δ-layers in atomic-scale devices. However, the 1Δ states have not been observed in these experiments, and it is therefore possible that we are lacking information which may be crucial to accurately modelling the behaviour of devices based on δ-layers. Results from the most recent experiment by Miwa *et. al.* [39] are presented in Figure 5.3. Figure 5.3a shows an ARPES measurement of a constant energy surface at the Fermi level, taken with $h\nu = 113$ eV. The accompanying LEED pattern is shown as an inset and the surface (1x1) unit cell is overlaid as a yellow square. Figure 5.3b shows an illustration of the theoretical predictions of the equivalent situation, reprinted from supporting online material accompanying Ref. [39]. The 1Γ and 2Γ states are predicted to arise in the zone centre, and the 1Δ states close the zone corners. In the measurements, a signal is clearly evident in the zone centre and recognised to arise from the 1Γ and 2Γ states. However, when comparing the two representations, it is clear that there is no evidence of the 1Δ states. A possible explanation for this may be that the 1Δ states are located above the Fermi level and would therefore not be observed by photoemission. This explanation is supported by the calculations presented in Figure 5.2, where the 1Δ states are shown to appear at a lower binding energy than the 1Γ and 2Γ states. It is therefore reasonable to assume that the 1Δ states may be unoccupied even though the Γ states are visible. Another possibility is that the 1Δ states are positioned beneath the Fermi level, but have not been found by the measurements due to other experimental factors.

The quantum well states are localised in the buried δ-layer and, due to the short mean free path of low kinetic energy photoelectrons, ARPES is a highly surface sensitive technique. It is therefore surprising that the quantum well states within such a buried layer are observable by ARPES at all, and the possibility of this was only recently demonstrated [36]. This is allowed by a resonant enhancement of the buried states such that the fraction of the wave function which exists near the surface may be measured. For the 1Γ and 2Γ states, this happens when probing with photon energies corresponding to electron emission from the bulk high symmetry X point. It is not given however, that this same photon energy will produce a resonance for the 1Δ states. When the 1Δ states do not appear in the measurements it may well be that the resonance point is not hit or that they simply do not have a resonance point. It must also be considered that the calculations may form an erroneous description of the situation, or that the interpretation of these calculations leads to an incorrect interpretation of where the 1Δ states should be located in the 2D Brillouin zone. The DFT calculations are constructed from a 4x4 supercell in order to integrate the phosphorus atoms in the lattice. This imposes a four times shorter periodicity on the calculated band structure. The band curvature must at the same time remain unchanged, as this would elsewise lead to a different electron effective mass. The resulting predictions will thereby be a *folded* representation of the real band structure. To recover the original structure, the bands need be untangled and refolded to their respective position. This process is not trivial, and may easily lead to a wrong prediction of different band locations.

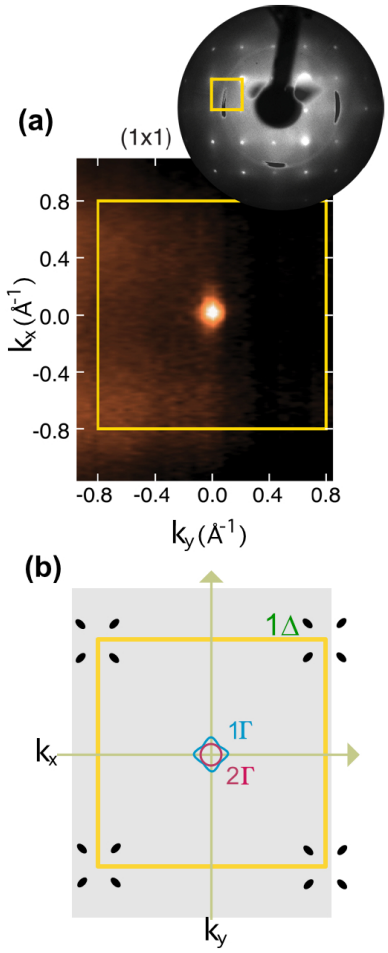

Figure 5.3: Recent experiment by Miwa *et. al.* [39]. Results show the Γ states, but the 1Δ states appear absent. (a) Fermi surface taken at $h\nu = 113$ eV with (b) accompanying schematics showing predicted positions for 1Γ, 2Γ and 1Δ.

5.2 Proposed Experimental Approach

Given that it is unclear whether the delta states simply do not exist, or whether the design of the previous experiments did not allow for the observation of these states, it is important to carefully consider any new approach.

There are two relevant experimental parameters that govern the location of the quantum well states relative to the Fermi level. These are the dopant density and the thickness of the dopant layer. With a higher density of phosphorus, more electron states are filled, and the Fermi level rises. The second parameter, the dopant layer thickness, dictates the confinement potential. In principle, for an infinitely thick film, the states 1Γ, 2Γ and 1Δ should behave as bulk, and therefore, as they are derived from the same bulk state, be equally occupied. As the dopant layer gets thinner, a confinement potential is created which effects the in-plane and out-of-plane states differently, separating the 1Γ, 2Γ and 1Δ states in terms of binding energy. The making of a thicker dopant layer should bring the states closer together, possibly revealing 1Δ states hiding above the Fermi level. In addition, it is experimentally easier to achieve the high-density limit with a thick dopant layer.

Motivated by these thoughts, samples of different character were prepared. Efforts were made towards making the samples with an equal high-density doping profile (25 % phosphorus), but with different dopant layer thickness. Not only is this a favourable approach for potential validation of the 1Δ states, it allows the effect of confinement to be monitored as the dopant layer decreases. Measurements were conducted on both buried and unburied δ-layers to investigate the effect of capping. Since it was not certain whether the 1Δ states were occupied states beneath the Fermi level, if they had a high symmetry point resonance, or even that they were located close to the 2D Brillouin zone corners, this could prove a severe and unfruitful task, particularly as the act of *not* observing the 1Δ states is not equivalent to disproving their existence.

5.3 Samples

The starting point for all samples was a p-type Si(001) wafer, prepared *in vacuo* by degassing at 650°C for several hours followed by flashing to 1200°C, to produce a clean and well-ordered surface. Preliminary measurements were conducted at this point to confirm the sample quality before continuing the dopant growth. This was accomplished by measuring the bulk bands by ARPES. A contaminated surface would break the sample periodicity, leading to non-conserved parallel

momentum in the photoemission process, leading to poor signal-to-noise and contributing to an overall broadening of the band linewidths. The detection of clear bands, as shown in Figure 5.4, is therefore testimony of a clean and well-ordered surface. The dopant layer was created with different procedures, depending on the desired thickness.

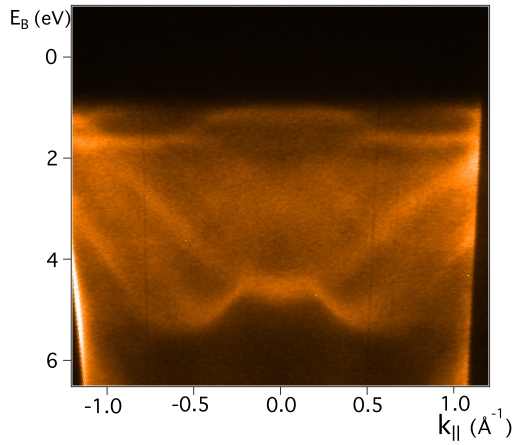

Figure 5.4: *Example measurement.* Clear bands indicating a clean, well-ordered surface.

To create a δ-layer confined to a single atomic plane, a *true* δ-layer, phosphine gas (PH_3) was dosed onto the sample for 5 minutes at a pressure of $P = 5 \cdot 10^{-9}$ mbar with the substrate at room temperature. This was followed by annealing to 350 °C for 10 seconds to remove hydrogen and incorporate the phosphorus to the surface. This procedure has been shown to make a coverage of $\frac{1}{4}$ monolayer of phosphorus at the sample surface [36]. To make a thicker dopant layer, Si was evaporated onto the substrate *at the same time* as the phosphine gas was dosed. As before, the phosphine was dosed at a base pressure of $P = 5 \cdot 10^{-9}$ mbar, and a Si filament was heated to evaporate for a total pressure of $P = 7 \cdot 10^{-9}$ mbar, until the layer had reached the desired thickness, based on the calculated silicon deposition rate. In this way, phosphorus will constantly be incorporated into the crystal, making up approximately $\frac{1}{4}$ of the lattice. A capping layer was created on two of the samples by evaporating Si on top for 20 minutes, corresponding to a coverage of 0.66 nm silicon, followed by a finishing anneal to reconstruct the surface.

Four different samples are illustrated in Figure 5.5. These are the *monolayer*, the *middle layer* and the uncapped and capped *megalayer*, appropriately named after the thickness of the dopant layer. The monolayer sample is a true δ-layer, with the dopants confined to a single atom plane, buried underneath a capping layer of silicon. The middle sample is uncapped, with a 2.0 nm dopant layer, created by simultaneous deposition of phosphine and silicon for one hour. Depositing for two hours, resulting in a dopant layer of 4.0 nm, one capped by silicon and one uncapped, created the megalayer samples. The calculations estimating these sample dimensions are provided in Appendix A.

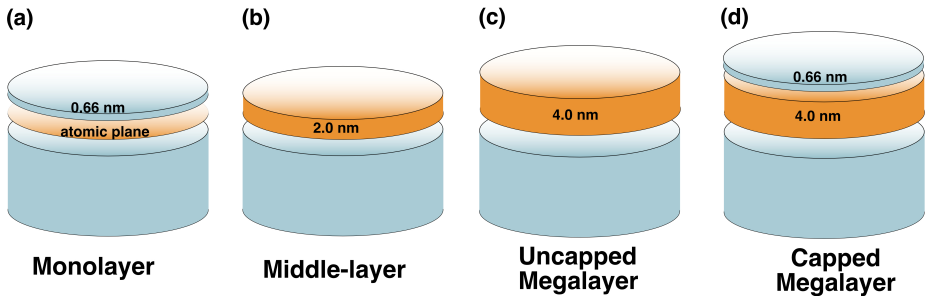

Figure 5.5: *Silicon samples.* Four samples of different dopant layer thickness was measured. Sample (a) was created with the doping profile as a "true" δ-layer, while the remaining three had thicker dopant layers. Samples (a) and (d) were capped by silicon.

5.4 Results and Discussion

As outlined in Section 5.2, a narrow potential force the quantum well states to split apart in terms of energy. The making of a thicker dopant layer should bring the states closer together. It is therefore a good approach to begin the investigation with the samples created with a 4.0 nm dopant layer, as, if the 1Δ states exist, this will bring them closer in energy to the already observed Γ states. Figure 5.6a presents a schematic of the Fermi surface, showing the predicted positions of the quantum well states[1]. The projected Brillouin zone is inset as a yellow square. The measured Fermi surface ($h\nu = 118$ eV) of the uncapped megalayer is presented in Figure 5.6b. In the zone centre, features that are interpreted to be the Γ states are recognised, and the shape of these suggests the presence of both 1Γ and 2Γ. In addition, there is a clear evidence of states located near the 2D zone corners, strikingly similar to the predicted 1Δ states. One interpretation is that these features derive from the bulk CBM, and are not associated with any quantum well states, but this explanation can be discredited. Firstly, the bulk CBM is calculated to reside well above the Fermi level (see Fig. 5.1). Secondly, the bulk CBM (located near the high symmetry X points) should manifest itself equivalently in all its six representations within the 3D Brillouin zone. Detailed ARPES measurements were carried out, comparing the out-of-plane (Figure 5.7b) and in-plane (Figure 5.7c) representations. Figure 5.7a provides an overview for the measured locations. The out-of-plane and in-plane features are captured at $\boldsymbol{k} = [0, 0, 3.3]$ Å^{-1} and $\boldsymbol{k} = [\pm 0.17, -1.1, 3.5]$ Å^{-1},

[1]The illustration is the equivalent of Figure 5.3a, rotated 45°, and with redefined directions of k_x and k_y, to match the experimental orientation.

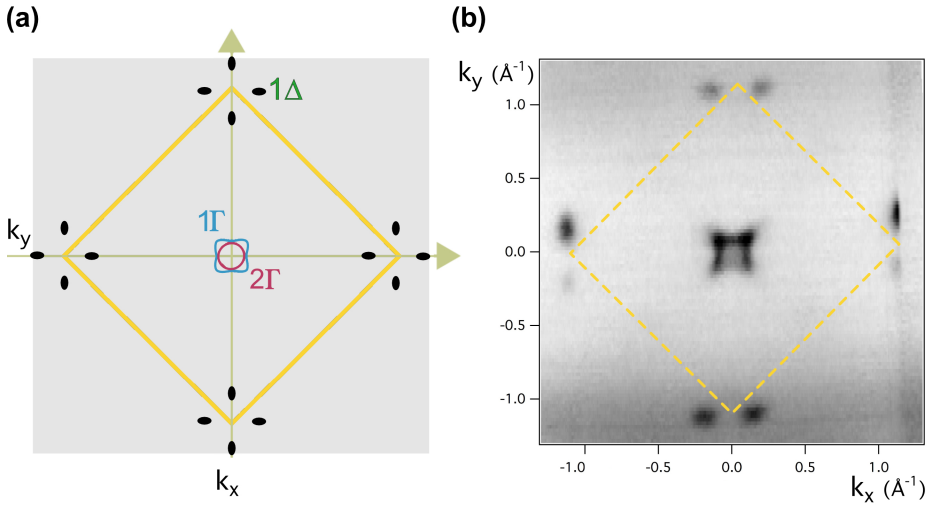

Figure 5.6: *Fermi surface.* (a) Re-adapted illustration of the Fermi surface from Ref. [38]. The predicted positions of the quantum well states, 1Γ, 2Γ and 1Δ are shown relative to the projected 2D Brillouin zone (yellow square). (b) Fermi surface measurements of the uncapped megalayer at $h\nu = 118$ eV.

respectively[2]. The equivalent coordinates given relative to their closest Brillouin zone centre is thus $\boldsymbol{k} = [0, 0, 1.0]$ Å^{-1} for the out-of-plane feature, and $\boldsymbol{k} = [\mp 1.0, 0, 0]$ Å^{-1} for the in-plane features. The former of these shows a band minima at $E_B = 195$ meV, while the latter appear with a binding energy of $E_B = 50$ meV. The measurements thus reveal that these states do *not* appear with equal binding energy, and should therefore not be attributed to the bulk CBM. The states obtained in the zone centre and 2D zone corners are therefore confidently identified to originate from the Γ bands and 1Δ band respectively.

Figure 5.7b reveals that the out-of-plane feature can be well described by the presence of a single parabola, with band minima at $E_B = 195$ meV. This parabola is presumed to contain both 1Γ and 2Γ, since we expect both these states to appear at a higher binding energy than the 1Δ state, and the latter is obtained at $E_B = 50$ meV. It is not unexpected that the valley splitting between 1Γ and 2Γ does not resolve in these measurements. The confinement in this sample is much less than for a true δ-layer, and only a narrow splitting between 1Γ and 2Γ is predicted in the latter.

[2]The value of $V_0 = 10.9$ eV is used for the inner potential, as measured for bulk silicon by Ashenford *et al.* [3].

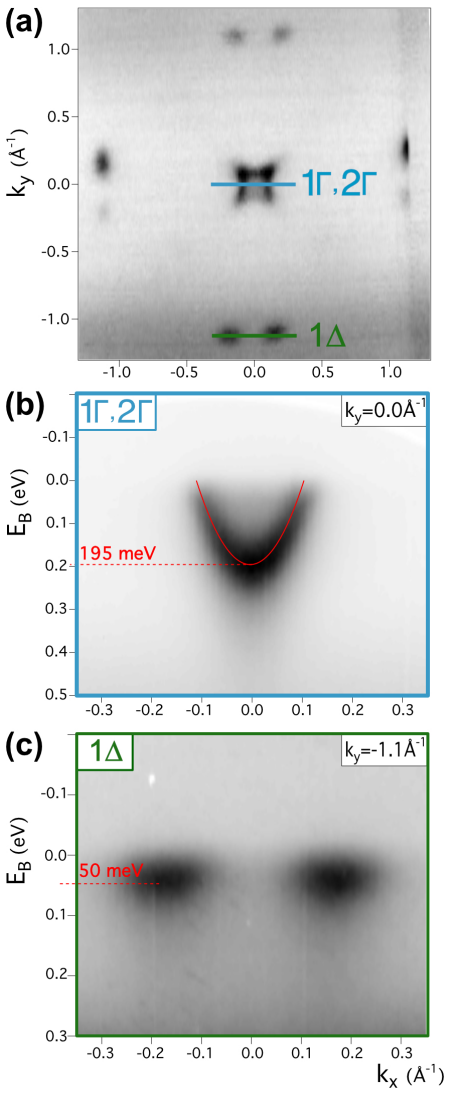

Figure 5.7: (a) Fermi surface at $h\nu$ = 118 eV. Blue and green lines indicate the orientation of measurements taken at (b) the zone centre, $h\nu$ = 36 eV, and (c) the projected 2D zone corners, $h\nu$ = 45 eV.

Going back to the Fermi surfaces of Figure 5.6, an interesting mismatch is evident between the predicted and the measured appearance of the 1Δ states. Where the 1Δ states are predicted to form a "flower" shape around the zone corners, only two of the "leafs" in this shape are present in the measurements. The reason for this is a resonant enhancement which occurs at some locations, enabling direct measurements of the states. That is, a strongly enhanced photoemission intensity occur when the electron initial state has a momentum that is well matched to that of a bulk-like final state into which it can be excited [36]. To understand how this effect explains the absence of the two "leafs", it is necessary to examine the 2D and 3D Brillouin zones.

Consider the illustration of Figure 5.8, showing the silicon bulk 3D Brillouin zone. Underneath is illustrated an extracted plane, cutting through the 3D zone centre, and spanning through the neighbouring zones. The *projected 2D Brillouin zone* (dotted blue lines in the underlying plane) takes the shape of a square. The bulk high symmetry X points are indicated in the 3D zone, and may be projected down to the plane. A state originating from the "top X" symmetry point will, as a result of the projection, be located at the centre of the 2D Brillouin zone. States originating from a "side X" symmetry point will, however, be projected to the 2D zone corners. An important note is that *equivalent* positions between 2D

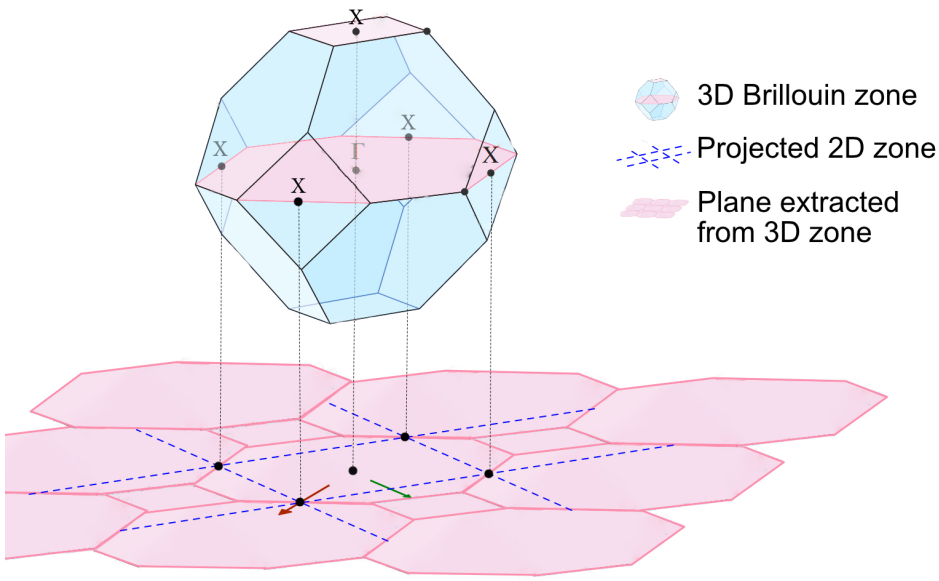

Figure 5.8: *Brillouin zone projection.* Silicon 3D Brillouin zone[3]showing high symmetry X points and their location in the projected 2D zone.

square zones may have *different* locations in the plane extracted from the 3D zone. As an example: The middle 2D square from the extracted plane is located within a red octagon. Upon travelling from this square to the next by traversing through a zone *corner* (dark red arrow) one will approach a 2D zone that is also inside a red octagon. On the other hand, by traversing through the square *side* (green arrow) one will end up in a 2D zone corresponding to an entirely different place in the extracted 3D plane. This now explains why only two of the 1Δ "leafs" are detected simultaneously. Even though we are scanning equivalent 2D initial states, they will not be matched to the same final state. Therefore, resonant enhancement does not occur for all 1Δ states simultaneously.

By measuring Fermi surfaces for a range of different photon energies, the positions for intensity enhancement of the quantum well states was revealed. These are illustrated by the schematics of Figure 5.9. The δ-layer states are non-dispersing with $k_\perp$, and appear as cylinders through the 3D Brillouin zone. It was found that the 1Γ and 2Γ states were resonantly enhanced when probing the high symmetry X-plane, while the 1Δ states experienced this effect in the high symmetry Γ-plane.

[3]Image of 3D Brillouin zone adapted from [37]. Reused in several figures.

Note how the 1Δ states (left cylinder) are always visible when appearing within a red octagon, whereas the Γ states (right cylinder) are visible when located in a red square. The resulting effect yields a pattern where, within each 2D zone (dotted blue square), either the 1Δ or the Γ states are detected from the photoemission process.

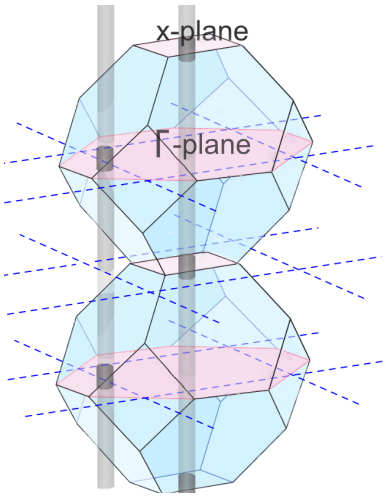

Figure 5.9: The varying intensity from the observed 2D states through the Brillouin zone.

Measurements obtained from the X-plane and the Γ-plane are presented in Figure 5.10a and 5.10b respectively. A comparison of the two clearly shows an inversion of the signal intensity. In Figure 5.10a the 1Γ and 2Γ appear strong in the zone centre, while the 1Δ states are not visible within the same zone. In Figure 5.10b, however, the opposite "set" of quantum well states are detectable. Here, the 1δ states are visible in the zone corners, while the Γ states are weakly present in the centre. The fact that the Γ states *do appear* in the centre of Figure 5.10b, outside its resonance point, serves as a confirmation of their dimensionality. Note that in the measurements, different pairs of the 1Δ states are brought to light, revealing all the different representations between them.

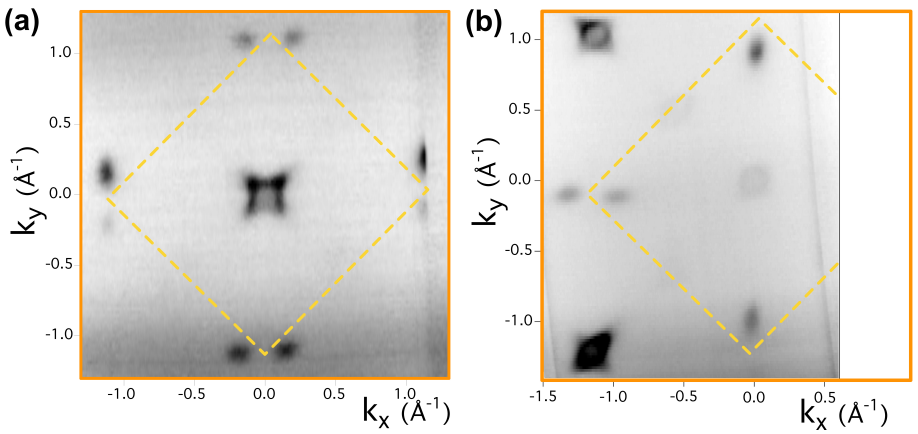

Figure 5.10: Fermi surface of the uncapped megalayer. Obtained at (a) the X-plane ($h\nu = 118$ eV), and (b) the Γ-plane ($h\nu = 80.5$ eV).

The thickness of the dopant layer in the discussed sample is estimated to be 4.0 nm. This is far from a true δ-layer, and it is interesting that the sample already shows formation of a two-dimensional electron gas. One can view a bulk-doped sample as the equivalence of an infinite δ-layer. For such a situation, the observed states should behave like bulk, 3D states, while in the opposite limit the states would be completely 2D. Upon creating δ-layers of different thickness, the transition from 3D to 2D becomes observable in incremental steps. The measured Fermi surface for four samples of different thickness is presented in Figure 5.11.

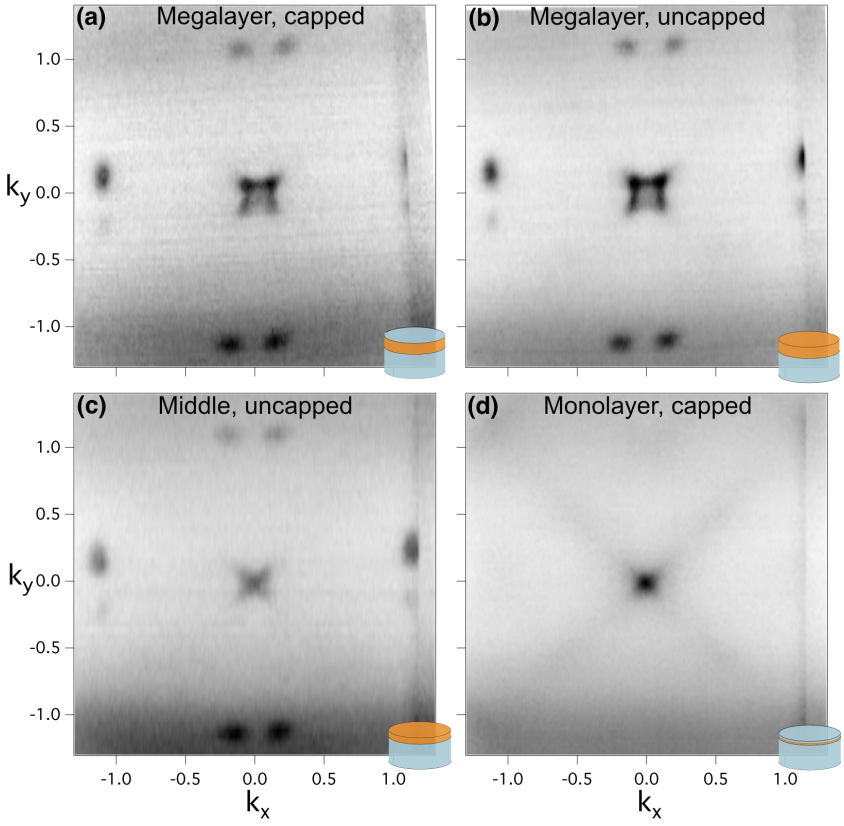

Figure 5.11: *Fermi map of all silicon samples.* Measurements taken at photon energy $h\nu = 118$ eV for direct comparison between the four different, (a) capped megalayer, (b) uncapped megalayer, (c) middle- and (d) monolayer sample.

The measurements are taken at photon energy $h\nu = 118$ eV, corresponding to

a cut through the X-plain indicated in Figure 5.9. Figure 5.11a and 5.11b are obtained from the capped and uncapped megalayer respectively. Figure 5.11c is from the middle sample and 5.11d presents the monolayer. Comparison of the capped and uncapped megalayer indicated that the burying of the δ-layer has little effect on the quantum well states. The measurements do not differ noticeably from each other, other than an expected reduction of the signal quality induced by burying the states. The capping layer is calculated to be approximately 0.6 nm, which corresponds to a coverage of about 6 atomic layers of silicon. This means that when detecting photoelectrons excited from the dopant layer, they will first need to traverse through several planes of silicon before crossing the surface/vacuum interface, thus weakening and distorting the signal.

A distinct difference between the monolayer and the remaining samples is observed, where the foremost mentioned seems to display an entirely separate pattern. The cause of this impression is twofold. Firstly; the 1Δ states are no longer visible, which will be addressed later. Secondly, a *streaking* has arisen, forming a cross through the image. The streaking are proven to be an effect from the surface Umklapp process. The silicon atoms will reconstruct at the surface, as they no longer have an overlaying plane of atoms to bond with. Typically, this reconstruction results in a (2 x 1) surface periodicity, and with a rotational equivalence of (1 x 2), the resulting periodicity will appear (2 x 2). As the unit cell gets twice as big, the reciprocal lattice vector becomes halved. Upon crossing the surface/vacuum interface, the electrons may now exchange parallel momentum with the lattice equal to half the bulk periodicity. Features from the original pattern will thereby be "copied", to form a resulting periodicity of half the original size. This effect is more easily recognised by going back to Figure 5.10b. Here, the Γ states are strongly appearing at $k_x = \pm 1.1$ Å^{-1}, $k_y = \pm 1.1$ Å^{-1}. By carefully examining the areas $k_x = \pm 0.55$ Å^{-1}, $k_y = \pm 0.55$ Å^{-1} we can indeed recognise a weak repetition of the Γ state features. This does not fully explain the streaking of Figure 5.11d, however, where the streaking is not a single repetition of an observed state, but rather two lines forming a cross through the measurements. This is simply understood by considering the effect if the surface rather reconstructed to appear (4 x 4). The Γ states will then be "copied" with a $\frac{1}{4}$ fraction of the original periodicity. Extending this principle to an even larger surface periodicity, it is clear that the eventual result will be an appearing cross, slicing through the zone centre. This means that the apparent discrepancy should not be associated with the δ-doping in itself, but that the surface reconstruction of the monolayer sample is less ordered than for the remaining samples. A detailed investigation of the surface Umklapp effect on Si:P δ-layers is provided by Ref. [39]

Figure 5.12 presents measurements of the Γ states for all four samples, with an

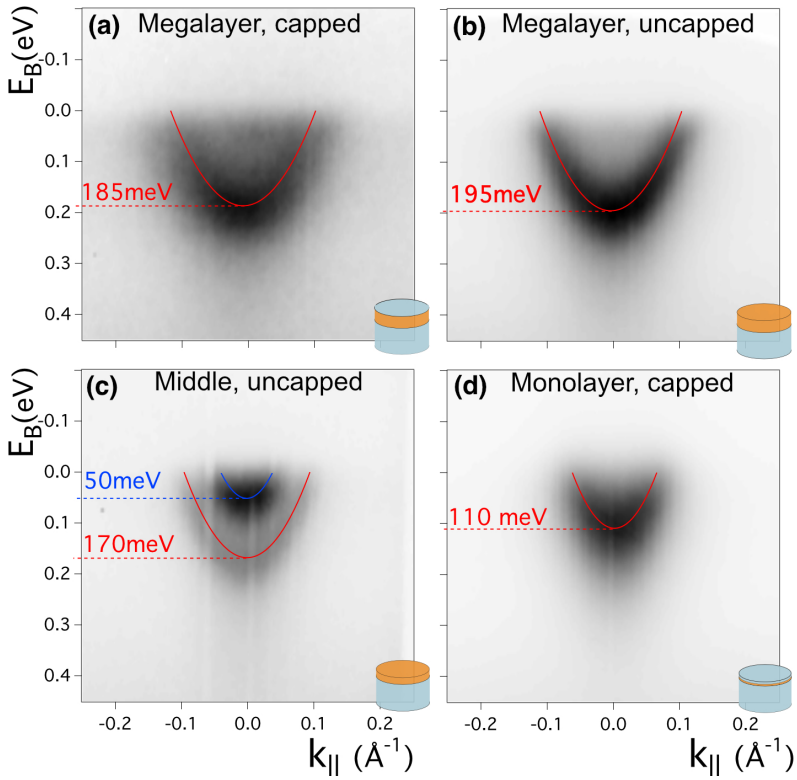

Figure 5.12: *Energy scan of all silicon samples.* Measurements of the 1Γ and 2Γ quantum well states in samples of different doping layer thickness. A parabola is fitted to the states, estimating the binding energy at $k_{\|} = 0$

overlaid parabolic trend. This is constructed by extracting horizontal (constantenergy) and vertical (constant momentum) slices through the measurements, and fitting a parabola to the intensity peak positions. This procedure [4] reveals that that two bands contribute to the total intensity from the middle-layer sample (Figure 5.12c), while the signal obtained from the remaining samples are well described by a single parabola. This is understood by the following arguments; The capped and uncapped megalayer samples show band minima of $E_B = 185$ meV and $E_B = 195$ meV respectively. Ref. [34] shows that a completely saturated $\frac{1}{4}$ ML phosphorus delta layer will give a binding energy of 200 meV for the 1Γ state. It is thus inferred that the megalayer samples are close to saturation.

[4] Elaborated in appendix B.

High dopant density, combined with a thick dopant layer, results in a deep, but wide, potential-well. This brings 1Γ and 2Γ deep beneath the Fermi level, but the confinement created is not narrow enough to split the states to a detectable separation. Thus, they appear degenerate. As the dopant layer becomes thinner, the confinement increases, and an observable splitting appear between 1Γ and 2Γ for the middle sample. The result is two distinct states, separated by a valley splitting of 120 meV. In the monolayer sample (Figure 5.12d), the band minima is obtained at binding energy of only $E_B = 110$ meV, thus the desired dopant density of $\frac{1}{4}$ fraction phosphorus atoms has not been reached. The potential well is not deep enough to bring both 1Γ and 2Γ below the Fermi level, so only 1Γ is visible[5].

Comparing Figure 5.12a and 5.12b it is clear that capping makes the detected signal weaker and noisier, as observed in the previous Fermi maps. This is a natural effect of burying the states, but is an expected consequence of our chosen method of probing these states and we cannot, based on the current data, infer whether this is also reflecting a physical change within the layer. A more notable difference is that the Γ states appear slightly deeper in the uncapped sample compared to the capped equivalent. This may indicate that the dopants are not confined within a sharp region of the sample, but diffuse into the bulk silicon. In the capped sample, the dopants are able to diffuse into silicon in both directions, while in the uncapped sample the dopants cannot diffuse into the vacuum. The doping profile of the uncapped sample will be the sharper of the two; making the Γ states appear with higher binding energy. Other effects could also contribute to this. Upon capping the sample, a different surface is introduced to the system, which again would create a new environment for surface states. This may result in separate effects of Fermi level pinning, which will also affect the measured binding energy.

Having characterised the 1Γ states of each sample, we now turn to examining the 1Δ states, which were observed in the constant energy slices. As it is expected that the strength of the confinement potential will change the splitting between all of the quantum well states, it is useful to consider the position of 1Δ relative to 1Γ. The 1Δ states are presented in Figure 5.13, where the binding energy is estimated by a Gaussian fit of the energy distribution curve (EDC), extracted along $k_{\|} = 0$. Both the capped (5.13a) and uncapped (5.13b) megalayer samples show the 1Δ states to be located at $E_B = 50$ meV. In the middle sample (5.13c) they are observed at a slightly larger binding energy, $E_B = 75$ meV, while in the monolayer sample (5.13d), the 1Δ states are not not observable beneath the

[5] All measurements have been performed at low temperature (8 K), reducing inaccuracy induced by thermal effects, and leaving the pixel size as the largest source of error. The error within determining these binding energies is estimated to be 10 meV (see appendix B).

Fermi level. A surprising result is that the quantum well states 1Δ and 1Γ are,

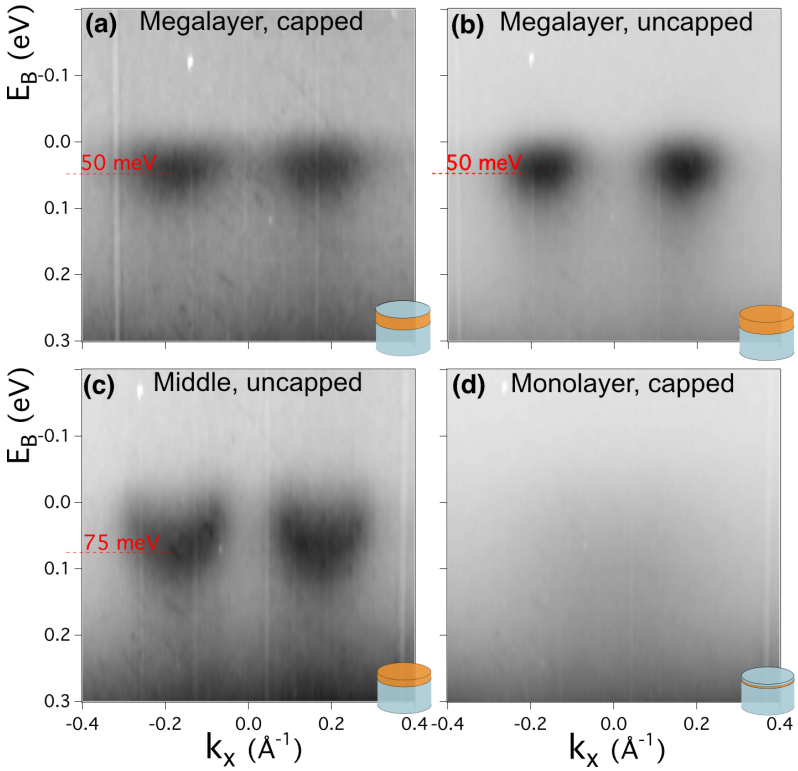

Figure 5.13: *Energy scan of all silicon samples.* Measurements of the 1Δ quantum well states in samples of different doping layer thickness. The states are obtained at $k_y = -1.1$ Å^{-1}.

in the middle sample, observed with a separation of only 95 meV. That is, the separation is *less* than that obtained for the thick samples (135 meV and 145 meV). The splitting is expected to behave inversely proportional to the sample thickness, making this an apparent contradiction. Several factors may create such a result, however. Firstly, experimental differences must be considered. While the megalayer samples are both from the same sample creation, measured before and after capping, the middle sample is produced from a different initial piece of bulk silicon. In the procedure of sample development, it is subject to several processes of annealing, flashing, and growth of both phosphorus and silicon. Silicon is a challenging material to maintain clean and well structured, and even small variations in the creation procedure may result in samples of different quality.

An explanation of more physical nature, however, is illustrated in Figure 5.14. As the dopant region becomes thinner, it eventually forces a splitting between the 1Γ and 2Γ bands. By reducing the extent of the dopant layer from 4.0 nm (megalayer) to 2.0 nm (middle sample), a valley splitting of 120 meV is induced between 1Γ and 2Γ. When this occur, it may simultaneously create a lowering of the 1Δ band, to house electron states suddenly pushed above the Fermi level by an abrupt raising of the 2Γ band.

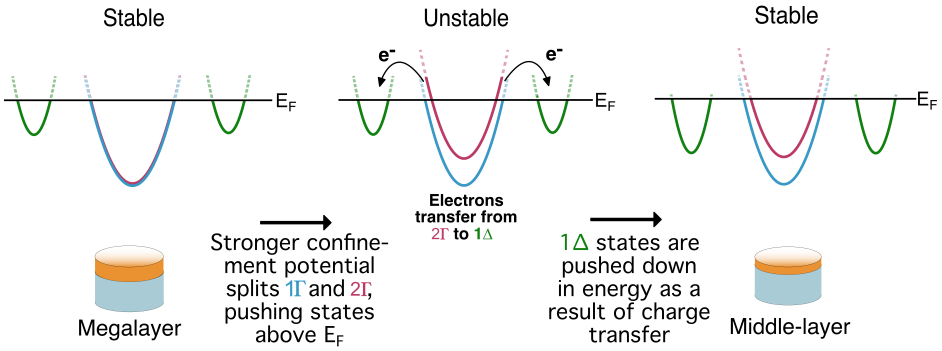

Figure 5.14: Illustration of the possible effect on the 1Δ states as the confinement potential increase by a thinner dopant region. 1Δ states are pushed down in energy as a result of charge transfer by a splitting of 1Γ and 2 Γ.

Currently, there is an increased drive internationally to realise a working quantum computer. This requires the engineering of suitable quantum states in a host material. These states must also be controlled, manipulated and read with atomic-scale precision. This experiment provides new insight into the nature of the quantum states created by Si:P δ-layers. Specifically, existence of the theoretically predicted 1Δ states is verified, discrediting suggestions that the states should emerge in a different location, or alternatively, not at all. It has been shown that confined states are formed with a 4.0 nm dopant profile. This led to very small splitting between the two most occupied bands, 1Γ and 2Γ. By further reducing the extent of the dopant layer to 2.0 nm, a valley splitting of 120 meV was induced between 1Γ and 2Γ, showing that the splitting may be controlled by changing the layer thickness. The verification of 1Δ now opens for a thorough investigation of the states characteristics. The results presented indicate that, while the splitting between states will increase with stronger confinement, the 1Δ states may be shifted down (in energy) when the confinement forces 1Γ and 2Γ to split apart. Investigation of this effect follows as a natural continuation to the work presented here, and as a further step towards complete understanding

of the quantum well states. The evidence of confinement already in samples with dopant layer as large as 4.0 nm motivates for another investigation. A bulk-doped sample can be viewed as the equivalence of an infinite δ-layer, in which, the observed states should behave like bulk, 3D states. In the opposite limit, a true δ-layer, the states would be completely 2D. When the dopant layer is 4.0 nm, confined states arise. However, it is not unlikely that the 1Γ, 2Γ and 1Δ states still inhibit *some* dependence on $k_\perp$. That is, the states may not be completely described as either 3D or 2D states, but something in between. Extending the approach adapted for this experiment could carry out investigation of this; creating samples of different dopant profiles thickness, to eventually reach bulk behavior, carefully mapping the $k_\perp$ dependence as the dopant layer increases.

Chapter 6

Diamond δ-doping

Experimental knowledge of the electronic band structure of diamond is relatively poor in comparison to semiconductors such as Si, Ge and GaAs [17], and even less is known about the band structure of thin film boron-doped diamond. Using angle-resolved photoemission spectroscopy, the electronic band structure of highly δ-doped layers within diamond is uncovered, investigating the effect of confinement and the usage of diamond in miniaturised systems. An introduction to the qualities of diamond and the advantages of thin film δ-layers will here be presented. This is followed by a description of the samples investigated, before the results obtained in this experiment is presented and discussed.

6.1 Previous works

Diamond exhibits an abundance of outstanding properties, such as high electronic carrier mobilities, high breakdown field strength and high thermal conductivity. It is one of the hardest materials existing in nature and shows itself to be robust against radiation damage [33]. These properties make diamond desirable for electronic devices of high voltage, high frequency and high power active and passive qualities [6]. With a band gap of around 5.5 eV, intrinsic diamond is highly insulating. Thus, in order to exploit diamond for electronic devices in room temperature, dopants with a sufficiently low thermal activation energy barrier need be incorporated into the system. Only boron and phosphorus have shown itself as reliable dopants, where the former is the most common of the two. At small doping concentrations, less than $5 \cdot 10^{17}$ cm^{-3}, boron creates an acceptor state

located at 0.37 eV above the valence band. Although this yield a lesser activation energy than by phosphorus doping (0.57 eV), this still only makes a fraction of the boron activated at room temperature, leading to a low concentration of free carriers [51]. However, increasing the boron concentration gradually decreases the activation energy, and an insulator-to-metal transition occur upon boron-doping concentrations exceeding $5 \cdot 10^{20}$ cm^{-3}, where a fully activated impurity band is formed. Heavily doping decrease the activation energy, but sadly it also decreases the carrier mobility as impurity scattering increases [6].

A solution to this problem came with the development of δ-doping diamond. By the epitaxial growth of a thin, heavily doped layer on the surface of (or buried within) a region of intrinsic or weakly doped diamond, a material of *both* high carrier concentration *and* high mobility can be created. The carriers are created by the heavily doped δ-layer and may be transported in the adjacent high-mobility layer, thus creating a new class of diamond electronic devices. However, investigations of such creations have led to varying conclusions surrounding the enhancement of the δ-layer systems compared to bulk diamond [4, 11, 43]. This may reside in the technological difficulty of creating a successful δ-layer, as it demands a very thin ($\approx$ 2 nm) region of heavily boron-doped diamond (preferably above the insulator-to-metal transition), with an atomically smooth interface to the intrinsic diamond. A recent paper by Butler *et al.* [6] showed significant progress in the fabrication process of δ-layer thin films and was able to demonstrate room temperature Hall effect mobility of 120 cm^2/Vs with a corresponding sheet carrier concentration of $1.3 \cdot 10^{13}$ cm^{-2}. This is an encouraging indicator of the possibility to obtain successfully δ-doped diamond with enhanced room temperature mobility, making this an appealing way for obtaining miniaturised devices with superlative qualities.

6.2 Samples

The results presented are mainly concerning two different diamond samples, one thin δ-doped sample and another bulk-doped diamond for comparison. The δ-layer sample consist of a thin ($\approx$ 1.8 nm) epitaxial layer of heavily boron-doped diamond, grown epitaxially on a weakly boron-doped substrate. The substrate is doped to a concentration of less than 10^{17} cm^{-3}. This value means that only a fraction of the boron present is activated at room temperature, leading to relatively low concentrations of free carriers in the bulk. The overlayer is doped to a concentration in the order of $\sim 10^{20}$ cm^{-3}, close to the insulator to metal transition to occur. This sample was compared with a semi-infinite heavily boron-doped sample, that is, a sample where more than the top 3 μm is boron-doped

to a concentration in the order of $\sim 10^{20}$ cm^{-3}. In addition, complimentary measurements are presented from a third diamond sample. This is created as to form a so-called *double δ-layer*, that is, two heavily boron-doped layers with weakly boron-doped diamond in between. Both δ-layers are 1.8 nm, with a spacing of 3.0 nm. The three diamond samples are illustrated in Figure 6.1.

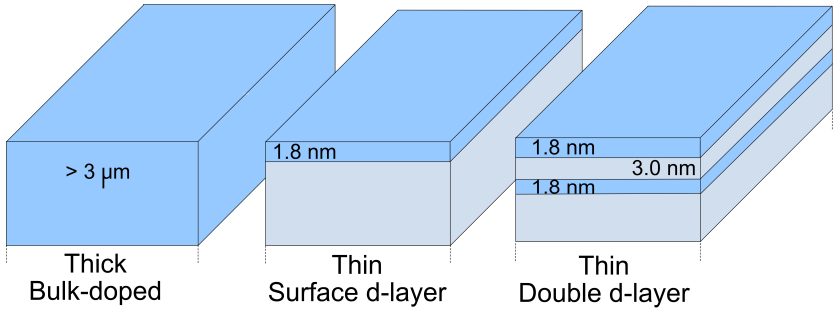

Figure 6.1: *Diamond samples.* Heavily boron-doped "thick" and "thin" diamond together with a "double δ-layer" sample. Grey colouring represent a doping concentration of less than 10^{17} cm^{-3}, while the blue areas illustrate a boron concentration in the order of 10^{20} cm^{-3}.

The cleaning process was done *in situ* by degassing at $T \approx 600$ K for several (8 - 12) hours. This ensures that water and other contaminants accumulate on the sample surface, to be removed by subsequent flashing procedures to $T \approx 1200$ K. The samples described have been the subject of thorough study to determine their different sample parameters. Further details about these samples can be found in Ref. [42] for the thick sample[1] and Ref. [6] for the thin, single and double δ-layer samples[2].

[1] Growth results are presented in Chapter 4.1 and the sample is named Sup1.
[2] The single and double δ-layer are referred to as sample 1 and 5 respectively.

6.3 Result and Discussion

The electronic band structure collected from the diamond samples has a somewhat different nature than the bands observed in silicon. The p-type doping with boron shifts the Fermi level down, thus resulting in an upward band bending. This means that the focus for the ARPES measurements will go from examining the conduction band, to now investigate the valence band. In turn, this proscribes a different approach in interpreting the measurements, as the possible induced quantum states must be untangled from the bulk valence band. It is therefore crucial to have a clear understanding of the bulk diamond band structure, in order to discern any relative changes in the δ-doped thin films.

Information about the electronic structure of the samples can be found by collecting ARPES data at different values of photon energy. That is, the band dispersion is repeatedly collected along the $k_{\parallel}$-direction, each image taken at a specific value of $k_{\perp}$. Measurements of bulk boron-doped diamond were collected in the range of $hv = 380$ eV to $hv = 580$ eV, where four of these are shown in Figure 6.2a-d.

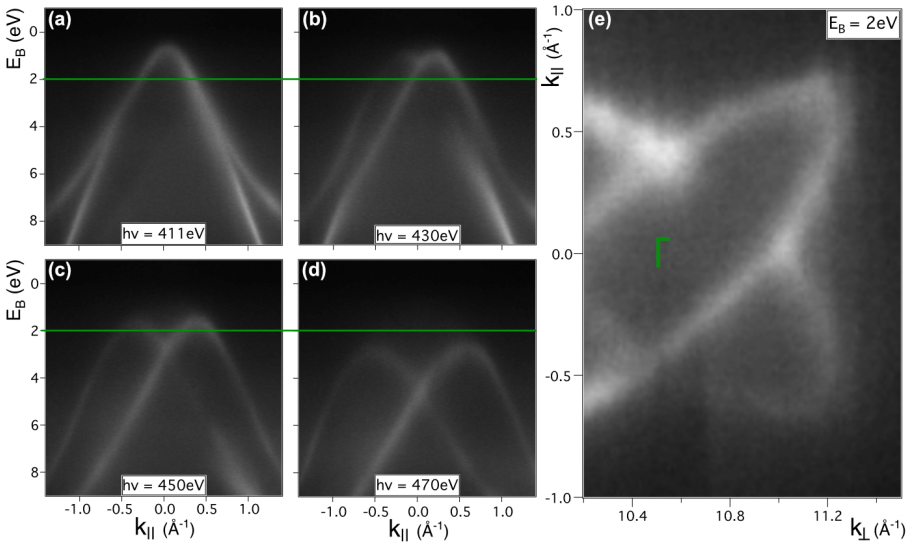

Figure 6.2: *Bulk boron-doped diamond.* (a-d) Band dispersion along $k_{\parallel}$, collected for four different photon energies. Closest cut through Γ is obtained for $hv = 411$ eV. (e) Constant energy surface at $E_B = 2$ eV.

Inspection of these images provides an understanding of the measured location in the Brillouin zone. The minimum binding energy at $k_{\|} = 0$ is obtained upon measuring with a photon energy of $h\nu = 411$ eV, making this the closest cut through the high symmetry Γ point. The bands here, shown in Figure 6.2a, falls nicely on top of each other at $k_{\|} = 0$, and split into two distinct bands for larger values of $k_{\|}$. This indicates that the measurement is cutting quite closely through Γ, and is an indicator of probing along the Γ-X direction. Increasing the photon energy will increase the value of $k_{\perp}$, while at the same time not affecting the collected value for $k_{\|}$, provided E_K is held fixed. This results in a movement throughout the Brillouin zone as illustrated by Figure 6.3. Note that the red lines, representing a single measurement, curve down in the BZ as $k_{\|}$ increase, in agreement with Eqn. 3.11. The measurements are collected in a range beginning slightly beneath the Γ point, to extend above the X point, as reflected by the figure.

By extracting a horizontal line from the single ARPES measurements, a constant energy surface may be created. This provides the dispersion of $k_{\|}$ as a function of $h\nu$. By demanding that the Γ point is mapped to $\Gamma_3 = 3[0, 0, \frac{4\pi}{a}] = [0, 0, 10.56]$ Å^{-1}, the inner potential is determined to $V_0 = 19$ eV. This is a reasonable value, and comparable to that provided by Guyot *et. al.* of $V_0 = 17.7$ eV [23], the value of 23 eV used by Yokoya *et al.* [60] and 22 eV experimentally obtained by Edmonds *et al.* [17]. After determining a value for the inner potential, the conversion from $h\nu$ to $k_{\perp}$ is possible. Such an image is displayed in Figure 6.2e, where a line at $E_B = 2$ eV (green line) is extracted from the single ARPES measurements. Electronic bands of a two-dimensional character are independent of $k_{\perp}$, and will appear as horizontal, dispersionless features in the image. The 3D bands, on the other hand, will disperse. In this way, the electronic dimension of the system may be unveiled. Studying Figure 6.2e, two bands is seen, forming a symmetric pattern around the Γ point. It is clear that the observed bands are dispersing with $k_{\perp}$, as neither is appearing as horizontal lines, confirming bulk behaviour for this sample

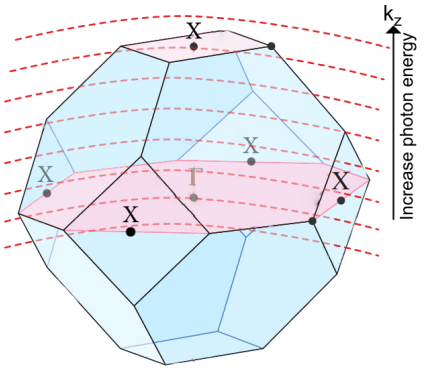

Figure 6.3: Location in the Brillouin zone corresponding to the measurements of Figure 6.2a-d. Each measurement is a curved cut through the Brillouin zone and increasing the photon energy correspond to increasing values of $k_{\perp}$.

There exists a large volume of theoretical and experimental work on bulk boron-doped diamond, as this material exhibit several outstanding qualities. Boron δ-doped diamond is now explored as a route to achieve high mobilities and carrier concentrations, and is desired for usage in miniaturised systems. However, little information is yet obtained concerning the electronic structure of such thin films. Figure 6.4 contributes to this missing information, presenting ARPES measurements of surface δ-doped diamond.

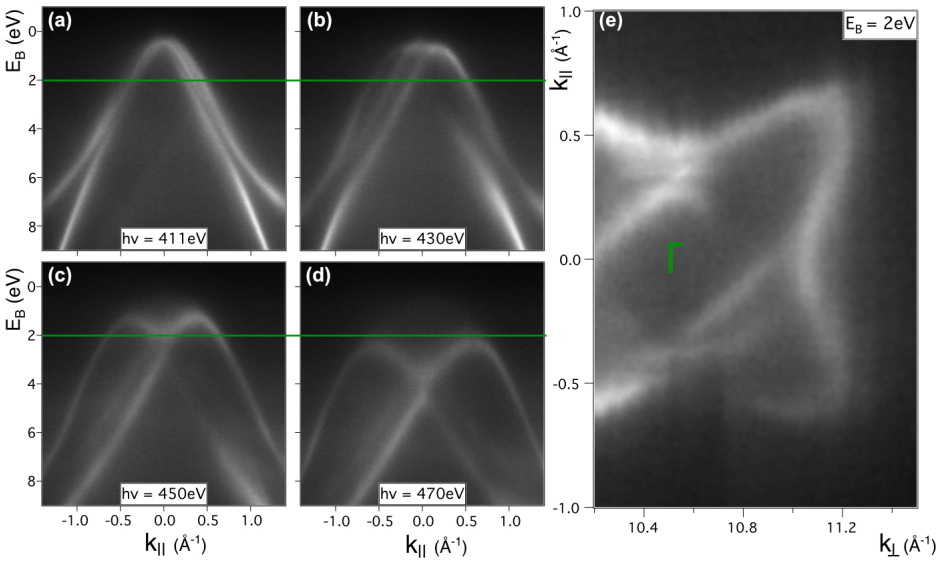

Figure 6.4: *Surface δ-doped diamond.* (a-d) Band dispersion along $k_{\parallel}$, collected for four different photon energies. Closest cut through Γ is obtained for $hv = 411$ eV. (e) Constant energy surface at $E_B = 2$ eV.

The measurements of Figure 6.4 do at first glance appear to have some qualitatively differences to that of the corresponding thick film data in Figure 6.2, where now three bands are distinctly visible. However, this additional band is not contributed to any quantum confinement effects. The band is not behaving electronically two-dimensional, as it then should appear as a horizontal line in Figure 6.4e. This band should rather be associated with a bulk band. Studying the band structure of bulk diamond, presented earlier in Figure 4.8b, it is clear that three bands are expected when probing in the Γ-K direction, which is exactly where this feature occurs. The presence of this band is therefore merely evidence of an increased sample quality, a notable advantage over the thick sample, but not an indication of new electronic behaviour from quantum confinement.

A closer inspection of the systems effective masses is presented in Figure 6.5. The ARPES measurements obtained at photon energy $hv = 411$ eV are shown, with blue and red schematics overlaying the surface δ-doped and the bulk sample respectively. The thin film is shown in Figure 6.5a, while Figure 6.5b presents the thick film. A comparison of the dispersions is provided in Figure 6.5c, where a vertical shift has been applied, to match the binding energy at $k_{\parallel} = 0$. The illustration shows high similarity between the two samples. If anything, there is a slight tendency towards a higher effective mass obtained for the electrons in the surface δ-doped sample. This is a somewhat crude estimate, as it is clear that the measurements of the thin film is not cutting perfectly through Γ. However, an investigation of the constant energy surface in Figure 6.4e reveals that a small miscut in this area would not affect the curvature of the bands notably. It is therefore concluded that no notable difference is observed for the systems effective masses.

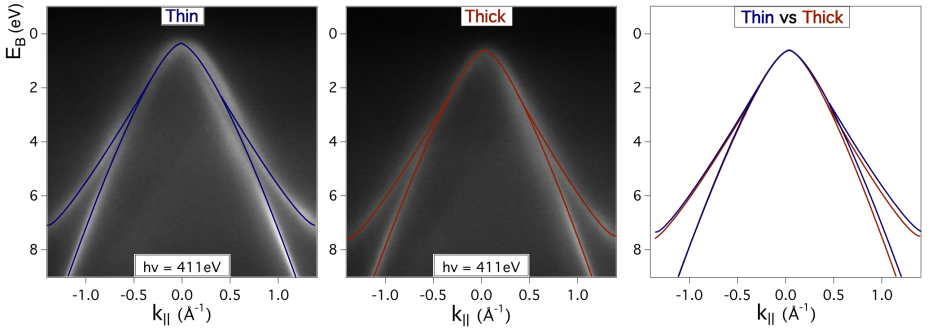

Figure 6.5: ARPES measurements obtained at photon energy $hv = 411$ eV with fitted schematics overlaid, showing the (a) δ-doped and (b) bulk sample. A vertical shift of the schematics is applied in (c) to match the binding energy at $k_{\parallel} = 0$.

Other than sample quality, the measurements presented so far show little difference between the surface δ-doped and bulk boron-doped diamond samples. Three bands have been recognised in the thin sample, all associated with bulk behaviour. Further investigation of the samples electronic properties is made possible by extracting the intensity along a constant value of $k_{\parallel}$ from the single ARPES measurements. That is, extracting a vertical cut trough the measurements, creating a waterfall plot. As before, 2D electronic bands are not dependent on $k_{\perp}$, and will in such a plot appear as vertical lines. A waterfall plot from surface δ-doped diamond is presented in Figure 6.6, integrating counts within the range $k_{\parallel} = [0.0, 0.2]$ Å^{-1} for improved statistics: this region of $k_{\parallel}$ is indicated on the band structure in

Figure 6.6c. Emission from the bulk band structure appear as the prominent feature, dispersing from the top lef to the bottom right of Figure 6.6a. In addition, a weak non-dispersive band is visible along $E_B = 0.9$ eV, indicated by a dotted blue line. It is clear that this feature is not dispersing with $h\nu$, and thus also not $k_\perp$, but appears at a constant binding energy regardless of which photon energy is used in the emission process. The electron states giving rise to this band is therefore not bulk-like, but have a two-dimensional character. Further investigation of this band was made by high statistics ARPES measurements, focusing on the range between $h\nu = 460$ eV and $h\nu = 480$ eV. The blue bar in Figure 6.6a marks this area, and the high statistics measurements are showed in Figure 6.6b. Here, the non-dispersive feature is clearly seen as an unchanging shoulder on the right hand side of the bulk band intensity. This state is, however, not suspected to arise from quantum confinement, but rather contributed to a surface state. This state, hereby named S1, has been reported in bulk boron-doped diamond by several sources [17, 15, 20], with all references reporting a constant feature at the Γ point.

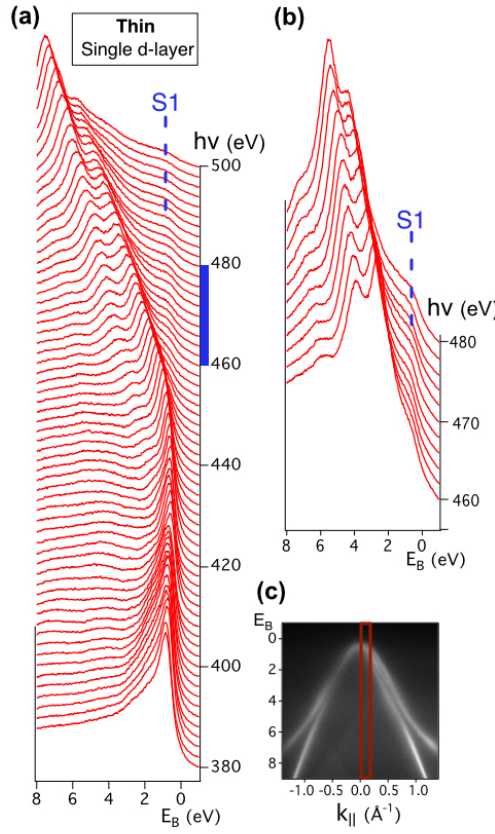

Figure 6.6: *Thin film diamond.* (a) Waterfall plot in the range $h\nu = 380 - 500$ eV, integrated between $k_\parallel = [0.0, 0.2]$. (b) High statistics measurements of the sub-range $h\nu = 460 - 480$ eV. (c) Image illustrating the integrated location.

Waterfall plots from the discussed bulk boron-doped and surface δ-doped diamond, in addition to the double δ-layer, are presented in Figure 6.7. From this presentation, it is clear that S1 is present in all three samples. In the thick sample (Figure 6.7a), S1 appears as a minor perturbance located at $E_B = 1.3$ eV, and is less visible that in the surface δ-doped sample (Figure 6.7b). S1 appears, however, most obvious in the double δ-layer, where it emerges as a strong vertical

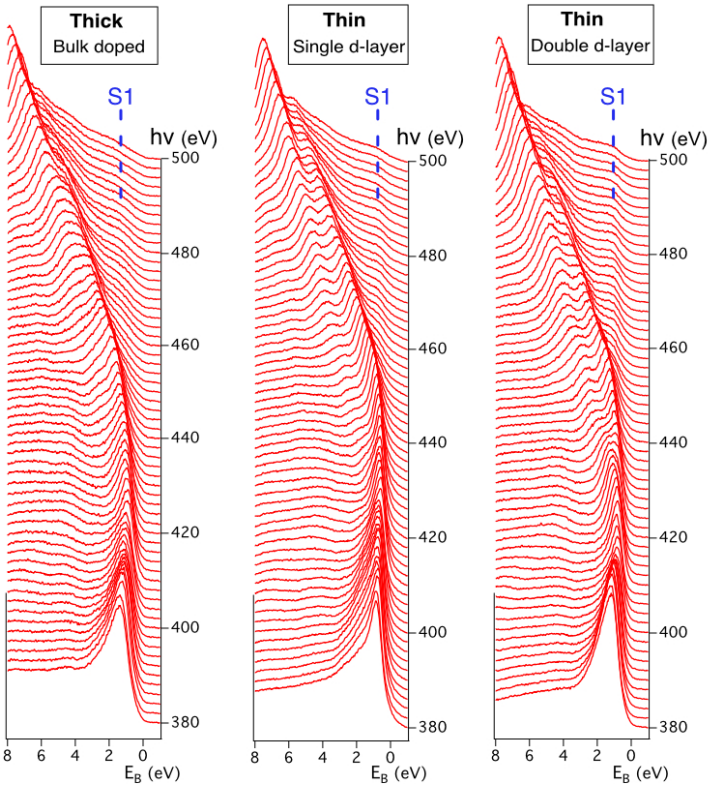

Figure 6.7: *All diamond samples.* Waterfall plot in the range $h\nu = 380 - 500$ eV, integrated between $k_{\parallel} = [0.0, 0.2]$. Measurements from (a) bulk boron-doped, (b) surface δ-layer, and (c) double δ-layer diamond. Surface state, S1, is present in all samples.

line along $E_B = 1.1$ eV. The strong presence of S1 in the two thin film samples, relative to the thick, is not an effect of confinement. This is clear, as S1 appears with different intensity, also between the two thin samples. The measured intensity naturally varies between samples, as small disturbances on the surface may greatly alter the signal. The *enhancement* of an electron state is not to be confused with the *creation* of an electron state. The former is associated with sample quality and measurement optimisation, while the latter would be a fundamental change of the material properties. Although it is with low intensity, the two-dimensional band is indeed present in the bulk sample, confirming S1 to be a surface state, which would be common to all the samples.

It is clear that the δ-doped diamonds are very similar to the bulk, in terms of the electronic bands dimensionality and the electron effective mass. All samples show the presence of the two-dimensional state S1, and no notable differences were observed by comparing the dispersion of the surface δ-doped sample to that of the bulk. Both the surface δ-layer and the double δ-layer showed a significant improved sample quality compared to the thick counterpart. This was evident by the detection of three bands in the Γ-K direction for the surface δ-layer, where only two bands were detectable in the thick sample, and the strong appearance of the surface state, S1, in both the single and the double δ-layer. This work shed light on the electronic band structure of thin film diamond, grown by creating highly doped δ-layers onto (and within) a weakly doped diamond substrate. The measurements indicates that bulk-like behaviour occurs for all samples, irrespective of their physical dimensionality. These results encourage the notion of using diamond in miniaturised systems, preserving diamonds desirable qualities also in atomic-scale devices.

6.4 Speculations

Although silicon and diamond share several crystallographic properties, the two materials responded quite differently to δ-doping. In silicon, two-dimensional states were already evident for a dopant layer of 4.0 nm, while δ-doped diamond, with a 1.8 nm heavily boron-doped epilayer, behaved strikingly similar to that of the bulk. The thin boron-doped layers do not exist at isolated films, but are grown on top of a substrate of weakly boron-doped diamond. Because of this, the wavefunction in the δ-layer regions are expected to extend further into the underlying diamond than it would for vacuum. The confinement is therefore less abrupt in these samples than it would be for a sample created as an isolated 1.8 nm thick layer. Nevertheless, this presents itself as a remarkable contrast to the behaviour observed in silicon. The reason for this seemingly converse reaction has been the subject of some discussion, which is summarised below.

An important difference between the δ-doping conducted on these materials, is the nature of the dopants used. The silicon dopant layer is produced by incorporating phosphorus, an n-donor creating a downward band bending, while the diamond thin film is heavily boron-doped, making it p-type. This would make an eventual upward band bending in diamond. In silicon, DFT calculations predict the quantum well states to reside in bands splitting off from the projected bulk conduction band, and as the work presented in Chapter 5 has shown, this prediction is validated by experimental data. The projected band structure in diamond

are illustrated by the simple schematics in Figure 6.8. The bands along the Γ-X and Γ-K direction is illustrated in the front of Figure 6.8a (red bands). By a translation parallel to the direction of $k_\perp$, through a distance of half a Brillouin zone, the band structure illustrated in green is reached. The red and green band diagrams thus represent a cut through the Γ-plane and X-plane respectively, as indicated by the Brillouin zone inset. The projected band structure is obtained by "merging" these planes together, including all the intermediate planes in the process. The result is shown by the shaded area of Figure 6.8b. Bands splitting upwards from the bulk band projection are illustrated in the figure by red dotted lines above the shaded projected bulk states. The calculated band splitting for silicon was predicted to strongly affect the conduction band minima. A proposed theory is that the band splitting will be the strongest along the Fermi contour which, in the case of diamond, occurs at the bulk Γ-point. This is reflected in Figure 6.8b, where the band splitting is indicated to be strongest at the valence band maxima. The opposite band bending therefore makes the Fermi contour between the two materials appear quite different, which may be of high importance for the resultant confinement effect.

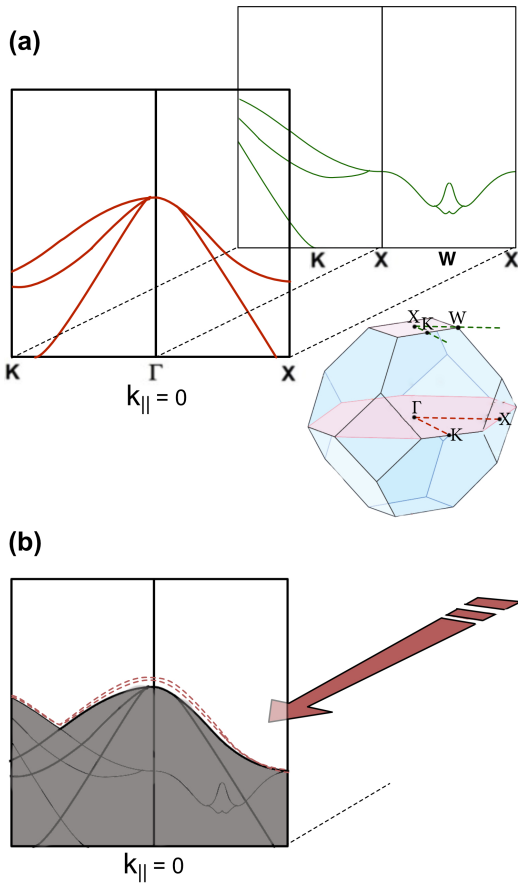

Figure 6.8: *Illustration of band structure projection.* (a) Diamond band structure in the Γ-plane and translated in $k_\perp$ to the X-plane. (b) Planes "merged" together, illustrating a projected band structure.

The silicon conduction band minima appears in the Brillouin zone as six valleys,

close to the zone X points. The diamond valence band maxima is, however, found in the zone centre, where the Fermi contour is small and approximately spherical. These situations are illustrated by Figure 6.9, where the described situation for silicon is shown in Figure 6.9a, and that of diamond in Figure 6.9b. Electronic confinement due to δ-doping will result in electron states independent of k_z. These states should therefore be fully described within the projected 2D Brillouin zone. This is visualised as a projection of the 3D Brillouin zone down to a 2D plane. The Fermi contour of silicon has a strong out-of-plane dependence, and such a projection greatly alters the appearance of the conduction band minimum valleys, where relative positions of the out-of-plane states have changed from the zone edge to be located in the zone centre. However, the same significant alteration is not forced upon the diamond, where the Fermi contour is small, spherical, and already located in the zone centre. Studying Figure 6.9b, it is evident that the characteristics of the valence band maxima are already closely related to the projected counterpart. In this way, it may be understood that an out-of-plane confinement have a strong effect on n-doped silicon, while a similar confinement does not alter the appearance of p-doped diamond.

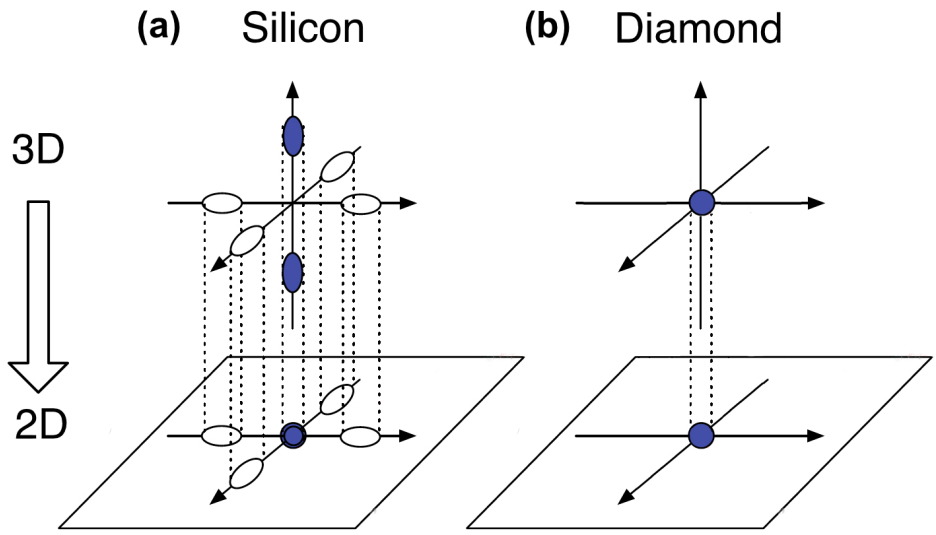

Figure 6.9: *Fermi contour projection.* Projection of the six conduction band minima valleys in silicon, and the valence band maxima in diamond, down to the 2D plane. The out-of-plane silicon valleys are strongly affected by the projection. Figure adapted from Ref. [31].

These thoughts should be considered as merely speculative, as they reside from

the assumption that the upward band splitting in diamond will be most affected in the valence band maxima. Even so, this provides an interesting starting point for further experimental investigations. Today, the effect induces by δ-doping is considered to mainly depend on the doping concentration and the width of the dopant layer. If the location of the Fermi contour is a contributing factor to such a vastly different response to confinement, then this also needs to be considered as a vital parameter when developing these δ-doped systems. This could experimentally be investigated by measuring n-doped diamond, or equivalently, p-doped silicon, where the latter may be the preferred approach, as phosphorus-doped diamond has a high activation energy, and has not yet been successfully grown at δ-layer thicknesses. Insight into how these materials respond to the opposite band bending, may provide information that either strengthen or discredit these speculations. One may also consider the approach of n-doping another material, where the conduction band minima is located at Γ, and compare this with the observed response of silicon n-type δ-doping.

Chapter 7

Conclusion

The effect of introducing electronic confinement in silicon and diamond with nanometer scale doping profiles, known as δ-doping, has been investigated, by using angle-resolved photoemission spectroscopy. Phosphorus δ-layers in silicon allowed a two-dimensional electron gas to be formed in the dopant layer. The effect of varying the dopant layer thickness was explored. It was found that confined states were formed with a 4.0 nm dopant profile, thicker than the typical thickness used in such studies. This led to very small splitting between the two most occupied bands, 1Γ and 2Γ, which have been the focus of previous work on this system. By further reducing the thickness of the dopant layer to 2.0 nm, a valley splitting of 120 meV was induced between 1Γ and 2Γ, showing that we can control the splitting by changing the layer thickness. The existence of theoretically predicted quantum well states, 1Δ, was verified experimentally for the first time. The location of these was shown to be in good agreement with density functional theory calculations. Through these results, the work presented here gives strength to established theoretical models, and provides an important step towards obtaining an accurate description of δ-layer derived devices. In order to realise a working quantum computer, engineered quantum states in a host material must be controlled, manipulated and read with atomic-scale precision. As this work provide new insight in the nature of the quantum well states induced by Si:P δ-layers, it also gives rise to new questions and motivates for further investigation. The results presented suggest that the 1Δ states shift towards higher binding energy upon the splitting of 1Γ and 2Γ. Deeper investigation of this effect follows as a natural continuation to the work presented here, and as a further step towards complete understanding of these quantum well states. The evidence of confinement in samples of 4.0 nm dopant layers, motivates for yet

another investigation: creating samples of even thicker dopant profiles to reach the final bulk, and in this way obtaining a complete transition from 3D to 2D behaviour.

Diamond is a material of superlative qualities, amongst other things showing high thermal conductivity, high breakdown field strength and being one of the hardest materials existing in nature. Boron δ-doped diamond is now explored as a route to achieve high mobilities and carrier concentrations, a critical requirement for implementing diamond in electronic applications. The investigation of doped diamond thin films is still in its youth, largely due to the lack of suitable dopants and the difficulties in creating such thin film samples. Recent progress in the fabrication process allowed for measurements of two high quality δ-doped diamonds to be conducted. These were created as a surface δ-layer and a double δ-layer, the latter with a buried δ-layer in addition to a layer at the surface. The effect of confinement was investigated by comparing the band structure obtained from the thin film samples to that of a highly boron-doped thick film. The measurements showed a surprising similarity between the δ-doped samples to that of the bulk counterpart, in terms of band structure and electron effective mass. This indicates that bulk-like behaviour occurs in all samples, irrespective of their physical dimensionality. These results encourage the notion of using diamond in miniaturised systems, preserving diamonds desirable qualities also in atomic-scale devices.

A discussion was presented exploring whether the nature of the Fermi contour may account for the stark contrast in the observed confinement effect between the two materials. The silicon CBM valleys are located far from the Brillouin zone centre, with a strong out-of -plane dependence, which may explain a resulting strong effect from an out-of-plane confinement. The VBM in diamond is, however, found in the zone centre, where the Fermi contour is small and approximately spherical. This may in turn result in a small induced effect of the confinement, as the characteristics of the VBM are not significantly different from its projected counterpart. These notions may be further examined by investigating the effect of an upward band bending in silicon or a downward band bending in diamond. At the present time the former approach is the more viable, as n-type doping of diamond is technologically difficult and has not yet been developed to the point where δ-layer thicknesses may be grown. Investigation of this effect will extend understanding of the requirements for forming engineered quantum states in semiconductor materials.

Appendices

Appendix A

Silicon Deposition Rate

The diamond samples have already been the subject of extensive preliminary measurements, providing sample parameters such as doping density and dimensions of bulk and δ-layers. The silicon samples were however created *in situ*, and thus a method for calculating the different layer thicknesses needed to be developed. This was accomplished by comparing the measured intensity from different atom core levels, tracking the rate of change as a function of deposition time and thus an increased thickness in the attenuating layer. Specifically, a layer of phosphorus was deposited on the sample and the P 2p core level was measured. Silicon was stepwise deposited on top of this, eventually burying the phosphorus. The phosphorus core level was measured between each step, making the calculation of the silicon growth rate possible.

The initial intensity, I_0, of the phosphorus core level and the resulting intensity, I_t, after deposition of silicon for t minutes are related by

$$I_t = I_0 e^{-\frac{d}{\lambda \cos\theta}}, \tag{A.1}$$

where λ is the inelastic mean free path of the electron and d is the overlayer thickness. The core level measurements were performed at normal emission ($\theta = 0$) and an assumed value of $\lambda = 0.7 \pm 0.1$ nm is adapted in accordance with the universal curve of inelastic mean free path. Rearranging Eqn. A.1, give the deposited silicon thickness after time t as

$$d = \lambda \ln \frac{I_0}{I_t} \tag{A.2}$$

The phosphorus core level was measured initially, after 2.5 minutes, 10 minutes, and lastly after 20 minutes of silicon deposition. To obtain comparable values for the measured core levels, the spectra need first be subject to a background removal. This distinguishes the electrons that are apparent in the measurement due to random scattering processes and those who should be identified with excitation from the measured core level. The background may be modelled in several ways, common choices being the linear, Shirley and Tougaard background. The foremost mentioned is the simplest model, but the latter two are considered more representative for the physical reality. In this calculation, the background is approximated by the Shirley model. The measured P 2p core levels, with a subtracted Shirley background, are shown in Figure A.1. The deposition rate is calculated assuming the ratio of total electron counts is equivalent to the ratio of core level intensity. Calculated deposition rate together with relevant parameters are summarised in Table A.1.

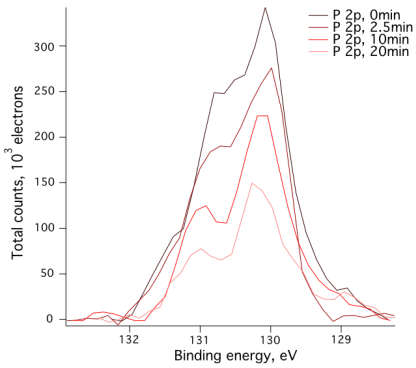

Figure A.1: Measured P 2p core level after depositing silicon for 0, 2.5, 10 and 20 minutes. Shirley background subtracted.

Table A.1: *Deposition thickness.* Every value for d is calculated relative to zero deposition.

t (minutes)	Total counts (10^6 electrons)	d (nm)	Deposition rate (nm/min)
0	3.32	0	-
2.5	2.64	0.16	0.065
10	2.06	0.33	0.033
20	1.30	0.66	0.033

The calculations show the deposition rate stabilised at 0.033 nm/min after silicon had been evaporated for at least 10 minutes. The rate of growth after 2.5 minutes was dramatically larger, with a value of 0.065 nm/min. This is interpreted as a burst of silicon when the evaporator first hits the correct temperature, skewing the rate. After some time, the growth will eventually trend to a constant rate. As the shortest deposition time of silicon was 20 min, the growth rate of 0.033

nm/min is used for all estimates of layer thickness. With an assumed uncertainty of 10% in the mean free path and the square root of counts in the value for the total counts, the estimated uncertainty in deposition rate is calculated to 0.0035 nm/min. The resulting descriptions of the silicon samples are presented in Table A.2.

Table A.2: *Sample description.* Thickness of phosphorus-doped δ-layers and the silicon capping

Sample name	δ-layer	Capping layer
Monolayer	$\frac{1}{4}$ monolayer	0.66 ± 0.07 nm
Middle	2.0 ± 0.2 nm	-
Thick, uncapped	4.0 ± 0.4 nm	-
Thick, capped	4.0 ± 0.4 nm	0.66 ± 0.07 nm

Appendix B

Parabolic trend for Γ states

In Chapter 5, measurements of the Γ states in silicon (Figure 5.12) were presented with an overlaid parabolic trend. The procedure for obtaining these parabola are illustrated by Figure B.1, where the middle δ-layer sample is used as an example. Figure B.1a show the obtained measurement. The EDC, extracted along $k_{||} = 0$ (black dashed line), is presented in Figure B.1b.

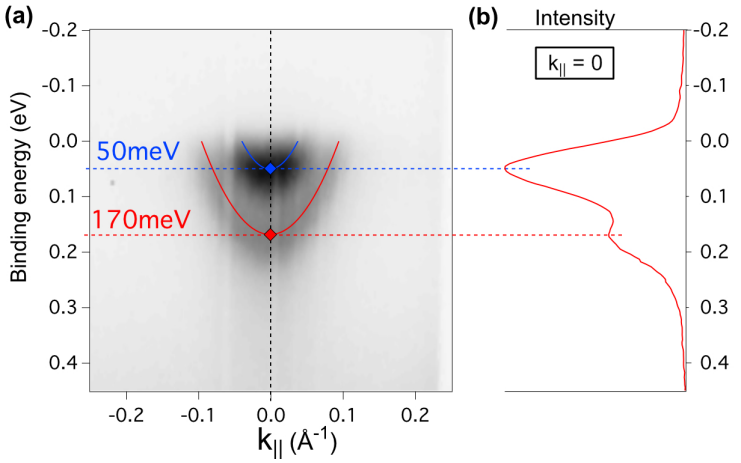

Figure B.1: (a) ARPES measurement of 1Γ and 2Γ states with (b) energy distribution curve extracted at $k_{||} = 0$. The position of the peaks is evaluated using a Gaussian, and used to create a parabolic trend for the Γ-states.

The intensity profile shows two distinct peaks, revealing that two bands are required to describe the Γ states. The peak positions, in terms of binding energy, were determined using a Gaussian fit. This procedure provides two data points, the centroid positions of the Gaussian peaks, connecting momentum and binding energy. These are marked in Figure B.1a with a red and blue diamond. A set of data points was collected by repeating this process for every EDC slice within a reasonable range. To increase the number of points for analysis, this process was repeated using momentum distribution curves (MDCs), intensity profiles extracted at constant binding energy. A parabolic trend-line has then been fit to these collected data points and overlaid on the collected data, allowing the dispersion of the Gamma state to be visualised.

The signals obtained from the remaining samples were described by a single parabola. This is discussed in Chapter 5, and interpreted to mean that splitting of the 1Γ and 2Γ states, if any, is less than the resolution of the measurements. All measurements regarding silicon was performed at low temperature (8 K). The error induced by thermal effects is therefore small ($\approx$ 2 meV), leaving the pixel size (5 meV) as the largest source of error. The total error for determining the band minima is estimated to be twice the pixel size, resulting in an error of 10 meV. Sources of error for the estimation of E_B are summarised in Table B.1.

Table B.1: Sources for error in estimating E_B for silicon Γ states.

source	$formula$	*error* (meV)
Thermal	$4k_BT$	2
Gaussian Fit	-	0.5
Fermi edge	-	1
Pixel size	2 x Width	10

Bibliography

[1] Als-Nielsen, J., and McMorrow, D. *Elements of Modern X-Ray Physics*, 2 ed. John Wiley & Sons Ltd, West Sussex, UK, 2001.

[2] Ashcroft, N. W., and Mermin, D. N. *Solid State Physics*. Harcourt, Inc, Orlando, 1976.

[3] Ashenford, D. E., and Lisgarten, N. D. The measurement of inner potential for diamond, germanium and silicon. *Acta Crystallographica Section A: Foundations of Crystallography 39*, 3 (may 1983), 311–314.

[4] Balmer, R. S., Friel, I., Hepplestone, S., Isberg, J., Uren, M. J., Markham, M. L., Palmer, N. L., Pilkington, J., Huggett, P., Majdi, S., and Lang, R. Transport behavior of holes in boron delta-doped diamond structures. *Journal of Applied Physics 113*, 3 (2013).

[5] Bianchi, M., Hatch, R. C., Mi, J., Iversen, B. B., and Hofmann, P. Simultaneous quantization of bulk conduction and valence states through adsorption of nonmagnetic impurities on Bi2Se3. *Physical Review Letters 107*, 8 (2011).

[6] Butler, J. E., Vikharev, A., Gorbachev, A., Lobaev, M., Muchnikov, A., Radischev, D., Isaev, V., Chernov, V., Bogdanov, S., Drozdov, M., Demidov, E., Surovegina, E., Shashkin, V., Davidov, A., Tan, H., Meshi, L., Pakpour-Tabrizi, A. C., Hicks, M. L., and Jackman, R. B. Nanometric diamond delta doping with boron. *Physica Status Solidi - Rapid Research Letters 11*, 1 (2017), 1–6.

[7] Carter, D. J., Marks, N. A., Warschkow, O., and McKenzie, D. R. Phosphorus δ-doped silicon: mixed-atom pseudopotentials and dopant disorder effects. *Nanotechnology 22*, 6 (feb 2011), 065701.

[8] Carter, D. J., Warschkow, O., Marks, N. A., and McKenzie, D. R. Electronic structure models of phosphorus δ -doped silicon. *Physical Review B 79*, 3 (jan 2009), 033204.

[9] Carter, D. J., Warschkow, O., Marks, N. A., and McKenzie, D. R. Electronic structure of two interacting phosphorus δ -doped layers in silicon. *Physical Review B 87*, 4 (jan 2013), 045204.

[10] Celli, F. Image of the SOLEIL synchrotron in Paris, France. Retrived from: http://www.gotscience.org/2015/12/nuclear-magnetic-resonance-a-dynamic-view-of-life/.

[11] Chicot, G., Tran Thi, T. N., Fiori, A., Jomard, F., Gheeraert, E., Bustarret, E., and Pernot, J. Hole transport in boron delta-doped diamond structures. *Applied Physics Letters 101*, 16 (oct 2012), 162101.

[12] Cooil, S. P. *Controlling the Epitaxial Growth of Graphene On Diamond Surfaces*. PhD thesis, Aberystwyth University, 2014.

[13] Cumpson, P. J., Seah, M. P., and Spencer, S. J. Calibration of Auger and X-ray photoelectron spectrometers for valid analytical measurements. *Spectroscopy Europe 3* (1998), 2–5.

[14] Damascelli, A. Probing the Electronic Structure of Complex Systems by ARPES. *Physica Scripta T109* (2004), 61–74.

[15] Diederich, L., Aebi, P., Küttel, O. M., Maillard-Schaller, E., Fasel, R., and Schlapbach, L. Surface-state dispersion of hydrogenated and hydrogen-free diamond (100) surfaces determined by angle-resolved photoemission. *Surface Science 393*, 1-3 (dec 1997), L77–L83.

[16] Drumm, D. W., Smith, J. S., Per, M. C., Budi, A., Hollenberg, L. C. L., and Russo, S. P. Ab Initio Electronic Properties of Monolayer Phosphorus Nanowires in Silicon. *Physical Review Letters 110*, 12 (mar 2013), 126802.

[17] Edmonds, M. T., Tadich, A., Wanke, M., O'Donnell, K. M., Smets, Y., Rietwyk, K. J., Riley, J. D., Pakes, C. I., and Ley, L. Valence-band structure and critical point energies of diamond along [100]. *Physical Review B - Condensed Matter and Materials Physics 87*, 8 (2013), 1–7.

[18] Fuechsle, M., Miwa, J. A., Mahapatra, S., Ryu, H., Lee, S., Warschkow, O., Hollenberg, L. C. L., Klimeck, G., and Simmons, M. Y. A single-atom transistor. *Nature Nanotechnology*, 7 (2012), 242–246.

[19] Geloni, G., Saldin, E., Schneidmiller, E., and Yurkov, M. Transverse coherence properties of X-ray beams in third-generation synchrotron

radiation sources. *Nuclear Instruments and Methods in Physics Research, Section A: Accelerators, Spectrometers, Detectors and Associated Equipment 588*, 3 (2008), 463–493.

[20] Graupner, R., Hollering, M., Ziegler, A., Ristein, J., Ley, L., and Stampfl, A. Dispersions of surface states on diamond (100) and (111). *Physical Review B 55*, 16 (apr 1997), 10841–10847.

[21] Griffiths, D. J. *Introduction To Electrodynamics*, 3 ed. Prenice-Hall, Inc, Upper, Saddle River, New Jersey, 1999.

[22] Griffiths, D. J. *Introduction to quantum mechanics*. Pearson Prentice Hall, 2005.

[23] Guyot, H., Achatz, P., Nicolaou, A., Le Fèvre, P., Bertran, F., Taleb-Ibrahimi, A., and Bustarret, E. Band structure parameters of metallic diamond from angle-resolved photoemission spectroscopy. *Physical Review B 92*, 4 (2015), 045135.

[24] Hofmann, P. *Solid state physics : An introduction*, 2 ed. Wiley-VCH Verlag GmbH & Co, 2015.

[25] Hofmann, P. *Surface Physics: An introduction*. No. Math 3630. Philip Hofmann, 2016.

[26] Hofmann, S. *Auger- and X-Ray Photoelectron Spectroscopy in Materials Science: A User-Oriented Guide*. Springer Verlag Berlin Heidelberg, Berlin, 2013.

[27] Hüfner, S. *Photoelectron spectroscopy: principles and applications*. Springer Verlag Berlin Heidelberg, Berlin, 2003.

[28] Karlsruhe Institute of Technology. SUL-X Beamline. Retrived from: www.anka.kit.edu/1629.php, 2015.

[29] Kittel, C. *Introduction to solid state physics*. John Wiley & Sons, Inc, Hoboken, 2005.

[30] Larmor, J. LXIII. On the theory of the magnetic influence on spectra; and on the radiation from moving ions. *Philos. Mag. Ser. 44*, 271 (1897), 503–512.

[31] Lee, S., Ryu, H., Campbell, H., Hollenberg, L. C. L., Simmons, M. Y., and Klimeck, G. Electronic structure of realistically extended atomistically resolved disordered Si:P δ -doped layers. *Physical Review B 84*, 20 (nov 2011), 205309.

[32] Mahan, G. Theory of Photoemission in Simple Metals. *Physical Review B 2*, 11 (1970), 4334 – 4350.

[33] Mazzola, F. *Photoemission spectroscopies and their application in solid state and material physics*. PhD thesis, NTNU, 2016.

[34] Mazzola, F., Polley, C. M., Miwa, J. A., Simmons, M. Y., and Wells, J. W. Disentangling phonon and impurity interactions in δ-doped Si(001). *Applied Physics Letters 104*, 17 (apr 2014), 173108.

[35] Mertens, K. *Photovoltaics : Fundamentals, Technology and Practice*. John Wiley & Sons Ltd, United Kingdom, 2014.

[36] Miwa, J. A., Hofmann, P., Simmons, M. Y., and Wells, J. W. Direct measurement of the band structure of a buried two-dimensional electron gas. *Physical Review Letters 110*, 13 (2013), 1–5.

[37] Miwa, J. A., Hofmann, P., Simmons, M. Y., and Wells, J. W. Supporting material: Direct Measurement of the Band Structure of a Buried Two-Dimensional Electron Gas. *Physical Review Letters 110*, 13 (2013).

[38] Miwa, J. A., Warschkow, O., Carter, D. J., Marks, N. A., Mazzola, F., Simmons, M. Y., and Wells, J. W. Supporting Online Material; Valley splitting in a silicon quantum device platform. *http://pubs.acs.org* (2014).

[39] Miwa, J. A., Warschkow, O., Carter, D. J., Marks, N. A., Mazzola, F., Simmons, M. Y., and Wells, J. W. Valley splitting in a silicon quantum device platform. *Nano Letters 14*, 3 (2014), 1515–1519.

[40] NextNano. Tight-binding band structure of bulk materials. Retrived from: Nextnano3/tutorial/1Dtutorial_TightBinding_bulk_GaAs_GaP.htm.

[41] Okazaki, H., Wakita, T., Muro, T., Nakamura, T., Muraoka, Y., Yokoya, T., Kurihara, S. I., Kawarada, H., Oguchi, T., and Takano, Y. Signature of high T c above 25 K in high quality superconducting diamond. *Applied Physics Letters 106*, 5 (2015), 5–8.

[42] Pakpour-Tabrizi, A. C. *Diamond Structures for Advanced Electronics*. PhD thesis, London Centre for Nanotechnology, 2017.

[43] Scharpf, J., Denisenko, A., Pakes, C. I., Rubanov, S., Bergmaier, A., Dollinger, G., Pietzka, C., and Kohn, E. Transport behaviour of boron delta-doped diamond. *physica status solidi (a) 210*, 10 (oct 2013), 2028–2034.

[44] Schofield, S. R., Curson, N. J., Simmons, M. Y., Ruess, F. J., Hallam, T., Oberbeck, L., and Clark, R. G. Atomically Precise Placement of Single Dopants in Si. *Physical Review Letters 91*, 13 (sep 2003), 136104.

[45] Schubert, E. F. *Delta-doping of semiconductors.* Cambridge University Press, Cambridge, UK, 1996.

[46] Schuegraf, K. K. *Handbook of Thin-Film Deposition Processes and Techniques - Principles, Methods, Equipment and Applications*, 2 ed. William Andrew Publishing, Norwich, NY, 2002.

[47] Seah, M. P., and Dench, W. A. Quantitative electron spectroscopy of surfaces: A standard data base for electron inelastic mean free paths in solids. *Surface and Interface Analysis 1*, 1 (feb 1979), 2–11.

[48] Simon, S. H. *The Oxford Solid State Basics*, 1 ed. Oxford University Press, New York, 2013.

[49] Singleton, J. *Band theory and electronic properties of solids*, 1 ed. Oxford University Press, New York, 2001.

[50] Suzuki, H., Harami, T., Miyahara, Y., Tokai, M., Naka, G., Ibaraki, K., Rizawa, T., Satoch, S., Tanabe, Y., Yoshiyuki, K., Nagafuchi, T., Kawazu, S., and Nakano, M. Development of 5-cell RF cavity for SPring-8 booster synchrotron. *Conference Record of the IEEE Particle Accelerator Conference.* (1991).

[51] Tokuda, N. *Novel Aspects of Diamond. Topics in Applied Physics: Homoepitaxial Diamond Growth by Plasma-Enhanced Chemical Vapor Deposition.* Springer International Publishing, Kanazawa, 2015.

[52] Tull, V. F. G. The Calculation of the Inner Potential of a Crystal. *Proceedings of the Royal Society of London A: Mathematical, Physical and Engineering Sciences 206*, 1085 (1951).

[53] Vinje, J. *Photochemistry of a Nucleobase Relevant to the Formation of Malignant Melanoma - Using Spectroscopic Techniques to Study the UV-Induced Damage of Thymine on MoS2.* NTNU, Trondheim, 2016.

[54] Wannberg, B. Hemispherical electron analyser. Retrived from: http://vgscienta.jp/wannberg-winner.html.

[55] Watson, T. F., Weber, B., Miwa, J. A., Mahapatra, S., Heijnen, R. M. P., and Simmons, M. Y. Transport in Asymmetrically Coupled Donor-Based Silicon Triple Quantum Dots. *Nano Letters*, 14 (2014), 1830–1835.

[56] Watts, J. F., and Wolstenholme, J. *An Introduction to Surface Analysis by XPS and AES.* John Wiley & Sons, Ltd, Chichester, UK, 2003.

[57] Willmott, P. *An Introduction to Synchrotron Radiation.* John Wiley & Sons, Ltd, Chichester, UK, 2011.

[58] Wilson, H. F., Warschkow, O., Marks, N. A., Curson, N. J., Schofield, S. R., Reusch, T. C. G., Radny, M. W., Smith, P. V., McKenzie, D. R., and Simmons, M. Y. Thermal dissociation and desorption of P H 3 on Si(001): A reinterpretation of spectroscopic data. *Physical Review B 74*, 19 (nov 2006), 195310.

[59] Wolf, S., and Tauber, R. N. *Silicon processing for the VLSI era, Vol. 1:Process Technology.* Lattice Press, 1986.

[60] Yokoya, T., Nakamura, T., Matsushita, T., Muro, T., Takano, Y., Nagao, M., Takenouchi, T., Kawarada, H., and Oguchi, T. Origin of the metallic properties of heavily boron-doped superconducting diamond. *Nature 438*, 7068 (2005), 647–650.

[61] Zabolotnyy, V. *Investigation of renormalization effects in high temperature cuprate superconductors.* PhD thesis, Technical University of Dresden, 2007.